



OPEN ACCESS

Characterization and Optimization of Skipper CCDs for the SOAR Integral Field Spectrograph

Edgar Marrufo Villalpando^{1,2} , Alex Drlica-Wagner^{2,3,4} , Andrés A. Plazas Malagón^{5,6} , Abhishek Bakshi³, Marco Bonati⁷ ,
Julia Campa⁸, Braulio Cancino⁷, Claudio R. Chavez^{3,9}, Juan Estrada³, Guillermo Fernandez Moroni³, Luciano Fraga¹⁰ ,
Manuel E. Gaido^{3,11}, Stephen Holland¹², Rachel Hur¹, Michelle Jonas³, Peter Moore⁷, and Javier Tiffenberg³

¹Department of Physics, University of Chicago, Chicago, IL 60637, USA; emarrufo@uchicago.edu

²Kavli Institute of Cosmological Physics, University of Chicago, Chicago, IL 60637, USA

³Fermi National Accelerator Laboratory, Batavia, IL 60510, USA

⁴Department of Astronomy and Astrophysics, University of Chicago, Chicago, IL 60637, USA

⁵Kavli Institute for Particle Astrophysics and Cosmology, Stanford University, Stanford, CA, USA

⁶SLAC National Accelerator Laboratory, Menlo Park, CA, USA

⁷Cerro Tololo Inter-American Observatory, NSF's National Optical-Infrared Astronomy Research Laboratory, Casilla 603, La Serena, Chile

⁸Departamento de Física, Universidad de Córdoba, Córdoba, España

⁹Universidad Nacional del Sur (UNS), Bahía Blanca, Argentina

¹⁰Laboratório Nacional de Astrofísica LNA/MCTI, 37504-364, Itajubá, MG, Brazil

¹¹Universidad de Buenos Aires, Facultad de Ciencias Exactas y Naturales, Departamento de Física, Buenos Aires, Argentina

¹²Lawrence Berkeley National Laboratory, One Cyclotron Rd, Berkeley, CA 94720, USA

Received 2023 October 9; accepted 2024 February 12; published 2024 April 11

Abstract

We present results from the characterization and optimization of Skipper charge-coupled devices (CCDs) for use in a focal plane prototype for the Southern Astrophysical Research Integral Field Spectrograph (SIFS). We tested eight Skipper CCDs and selected six for SIFS based on performance results. The Skipper CCDs are $6k \times 1k$, $15 \mu\text{m}$ pixels, thick, fully depleted, p -channel devices that have been thinned to $\sim 250 \mu\text{m}$, backside processed, and treated with an anti-reflective coating. We demonstrate a single-sample readout noise of $< 4.3 e^- \text{ rms pixel}^{-1}$ in all amplifiers. We optimize the readout sequence timing to achieve a readout noise of $0.5 e^- \text{ rms pixel}^{-1}$ after 74 non-destructive measurements, which can be accomplished in a region covering 5% of the detector area in a readout time of < 4 minutes. We demonstrate single-photon-counting in all 24 amplifiers (four amplifiers per detector) with a readnoise of $\sigma_N \sim 0.18 e^- \text{ rms pixel}^{-1}$ after $N_{\text{samp}} = 400$ samples, and we constrain the degree of nonlinearity to be $\lesssim 1\%$ at low signal levels ($0 e^-$ to $50 e^-$). Clock-induced charge (CIC) remains an important issue when the Skipper CCD is configured to provide a large full-well capacity. We achieve a CIC rate of $< 1.45 \times 10^{-3} e^- \text{ pixel}^{-1} \text{ frame}^{-1}$ for a full-well capacity of $\sim 900 e^-$, which increases to a CIC rate of $\sim 3 e^- \text{ pixel}^{-1} \text{ frame}^{-1}$ for full-well capacities $\sim 40,000$ – $65,000 e^-$. We also perform conventional CCD characterization measurements such as charge transfer inefficiency (3.44×10^{-7} on average), dark current ($\sim 2 \times 10^{-4} e^- \text{ pixel}^{-1} \text{ s}^{-1}$), photon transfer curves, cosmetic defects ($< 0.45\%$ “bad” pixels), and charge diffusion (point-spread function $< 7.5 \mu\text{m}$) to verify that these properties are consistent with expectations from conventional p -channel CCDs used for astronomy. Furthermore, we provide the first measurements of the brighter-fatter effect and absolute quantum efficiency ($\gtrsim 80\%$ between 450 and 980 nm; $\gtrsim 90\%$ between 600 and 900 nm) using Skipper CCDs.

Unified Astronomy Thesaurus concepts: [CCD observation \(207\)](#); [Astronomical detectors \(84\)](#); [Spectroscopy \(1558\)](#)

1. Introduction

Charge-coupled devices (CCDs) have revolutionized photon detection in scientific applications since their invention in 1969 (Amelio & Tompsett 1970; Boyle & Smith 1970; Damerell et al. 1981; Janesick 2001). CCDs rely on the photoelectric effect to

generate electron–hole pairs from incident photons on a silicon substrate. CCDs have been widely used in ground- and space-based astronomy due to their well-characterized performance, achieving quantum efficiencies $> 90\%$, dynamic ranges of $\sim 10^5 e^-$, and high radiation tolerance, while providing large fields of view, adequate spatial resolution, and moderate energy resolution (e.g., Janesick 2001; Gow et al. 2014).

Precision astronomical measurements with CCDs, particularly in the low signal-to-noise regime, have been limited by

 Original content from this work may be used under the terms of the [Creative Commons Attribution 3.0 licence](#). Any further distribution of this work must maintain attribution to the author(s) and the title of the work, journal citation and DOI.

the electronic readout noise which couples to the CCD’s output video signal (Janesick 2001). In the case of astronomical spectrographs, where light is dispersed over a large detector area, observations of faint sources will result in low signal-to-noise in each detector pixel. Detector readout noise can be an important contribution to the overall noise in an observation in this low-signal regime, affecting the sensitivity of spectroscopic measurements (Drlica-Wagner et al. 2020). Skipper CCDs provide a novel solution to the problem of detector readout noise. Skipper CCDs differ from conventional CCDs in the output readout stage; these devices use a floating gate amplifier to perform repeated, independent, non-destructive measurements of the charge in each pixel. Each independent charge measurement performs correlated double sampling (CDS) of the baseline and signal, thus suppressing low-frequency noise in order to achieve photon-counting capabilities. For uncorrelated Gaussian noise, the effective readout noise distribution after averaging multiple non-destructive measurements (or samples) per pixel is given by

$$\sigma_N = \frac{\sigma_1}{\sqrt{N_{\text{samp}}}}, \quad (1)$$

where σ_1 is the single-sample readout noise (the standard deviation of pixel values with a single charge measurement per pixel), N_{samp} is the number of measurements performed for each pixel, and σ_N is the noise achieved after averaging the measurements (e.g., Tiffenberg et al. 2017).

The Skipper CCD concept as a photosensitive detector was proposed in 1990 (Chandler et al. 1990; Janesick et al. 1990); however, in early demonstrations of this technology, the readout noise improvement deviated from the theoretical expectation at $\sim 0.5 \text{ e}^- \text{ rms pixel}^{-1}$ after 512 measurements per pixel (Janesick et al. 1990). Additional measurements did not yield further noise improvements, implying that systematic noise effects were preventing single-photon-counting (Janesick et al. 1990; Holland 2023). In contrast, modern Skipper CCDs have achieved readout noise and stable performance an order of magnitude lower over a large area detector (Tiffenberg et al. 2017).

While modern ultra-low noise, photon-counting Skipper CCDs have found abundant applications as particle detectors with extensive use in dark matter (DM) searches (e.g., Crisler et al. 2018; Barak et al. 2020; Aguilar-Arevalo et al. 2022; Cervantes-Vergara et al. 2023), they have not yet been used for astronomical observations due primarily to their long readout times. However, Skipper CCDs are expected to maintain the beneficial characteristics of conventional p -channel CCDs used for astronomy (e.g., stability, linear response, large dynamic range, high quantum efficiency, and radiation tolerance) since the only appreciable difference is the Skipper CCD output stage (Holland 2023). This makes them an attractive candidate technology for single-photon counting astronomy at optical/near-infrared wavelengths (e.g., Rauscher et al. 2022).

We intend to demonstrate the performance of modern Skipper CCDs for astronomical spectroscopy using the Southern Astrophysical Research (SOAR) Telescope Integral Field Spectrograph (SIFS). SIFS is a fiber-fed integral field spectrograph equipped with 1300 fibers, covering a $15 \times 7.8 \text{ arcsec}^2$ field-of-view with an angular resolution of $0''.30 \text{ fiber}^{-1}$ (Lepine et al. 2003; de Oliveira et al. 2010; Macanhan et al. 2010). For SIFS, the signal and background rates are expected to be $0.012 \text{ e}^- \text{ pixel}^{-1} \text{ s}^{-1}$ and $0.008 \text{ e}^- \text{ pixel}^{-1} \text{ s}^{-1}$, respectively. Since the signals are faint and the background contribution is small, SIFS can take advantage of the ultra-low-noise capabilities of the Skipper CCD and allow this technology to be exposed to the full complexities of astronomical spectroscopy for the first time.

Here, we present results from the laboratory characterization and optimization of eight astronomy-grade Skipper CCDs (“AstroSkippers”), which will be used for a Skipper CCD focal plane prototype for SIFS (Villalpando et al. 2022). These AstroSkippers are similar to Skipper CCDs developed for DM experiments (e.g., Barak et al. 2020), but have been thinned and backside processed for applications in astronomy. Here we perform a suite of characterization and optimization studies with a specific focus on optimizing readout time, readout noise, full-well capacity, and clock-induced charge (CIC). We present several measurements that are uniquely enabled by the single-photon resolution of the Skipper CCD (i.e., photon counting performance and low-signal level nonlinearity) as well as a suite of conventional CCD measurements that confirm that Skipper CCDs perform similarly to other thick, fully depleted p -channel CCDs. While reducing the readout time and the CIC at large full-well capacity remains challenging, our results verify the readiness of the AstroSkipper CCDs for on-sky testing.

This paper is structured as follows. In Section 2, we describe the physical characteristics and packaging of the AstroSkipper detectors. Section 3 describes the laboratory setup used to test detectors and outlines the characterization and optimization procedures. In Section 4, we describe the process for optimizing readout time with respect to noise and the detector area in order to achieve viable operation speeds for astronomical applications. Section 5 presents results on photon-counting performance and nonlinearity at low-signal levels. Section 6 describes voltage optimization procedures to achieve large full-well capacities while minimizing the CIC and maintaining photon-counting capabilities. In Section 7, we report the results of conventional CCD characterization tests including charge transfer inefficiency (CTI), dark current (DC), photon transfer curves (PTC), brighter-fatter effect (BFE), cosmetic defects, charge diffusion, and absolute quantum efficiency (QE) measurements. We conclude in Section 8 by summarizing our findings and outlining ongoing work to further optimize Skipper CCDs for astronomical applications.

2. AstroSkipper

Skipper CCDs have applications in a wide variety of particle physics measurements (e.g., Rodrigues et al. 2021; Botti et al. 2022; Fernandez-Moroni et al. 2022). The ultra-low noise of the Skipper CCD allows for the precise measurement of the number of free electrons in each of the million pixels across the CCD. This capability, combined with low background rates, has allowed Skipper CCD direct DM detection experiments to place world-leading constraints on DM-electron interactions (Crisler et al. 2018; Barak et al. 2020; Arnquist et al. 2023). These successes have led to extensive Skipper CCD research and development (R&D) for a planned multi-kilogram detector (Aguilar-Arevalo et al. 2022; Cervantes-Vergara et al. 2023).

In contrast, the application of Skipper CCDs to astronomy and cosmology is in a relatively early stage. In Drlica-Wagner et al. (2020), we performed the first optical characterizations of a Skipper CCD, designed at Lawrence Berkeley National Laboratory (LBNL), fabricated at Teledyne DALSA, and packaged at Fermi National Accelerator Laboratory (Fermilab) for cosmological applications. Results showed that the backside illuminated, 250 μm thick Skipper CCD could achieve relative QE $> 75\%$ from 450 to 900 nm, a full-well capacity of 34,000 e^- , and CTI $< 10^{-5}$. These competitive characteristics motivated the plans to test the Skipper CCD in a realistic astronomical observing scenario. In Villalpando et al. (2022), we described plans for installing a Skipper CCD focal plane prototype on SIFS to achieve the first astronomical measurements with these novel detectors. Here, we summarize results from testing large-format Skipper CCDs for astronomy (“AstroSkippers”) at Fermilab prior to installation at SOAR.

2.1. Detector Characteristics

We fabricated eight backside illuminated AstroSkipper CCDs for the SIFS focal plane prototype. These detectors came from a fabrication run supported by the DOE Quantum Science Initiative, Early Career Award, and laboratory R&D funds. Figure 1 shows one of these wafers, which was fabricated at Teledyne DALSA. The wafers were processed to reach astronomy-grade qualifications following the same procedure as used for the Dark Energy Camera (DECam) and Dark Energy Spectroscopic Instrument (DESI; Holland et al. 2003; Bebek et al. 2015, 2017; Flaughner et al. 2015). Factors such as thickness and CCD surface coatings were developed to reach high QE from the near-infrared (NIR) to the near-ultraviolet, which are desirable for astronomical observations (Bebek et al. 2015). The wafers were thinned from a standard thickness of 650–675 μm to 250 μm at a commercial vendor and then backside processed at the LBNL Microsystems Laboratory. A thin (20–25 nm) in situ doped polysilicon layer was applied to form a backside n^+ contact (Holland et al. 2007; Groom et al. 2017).

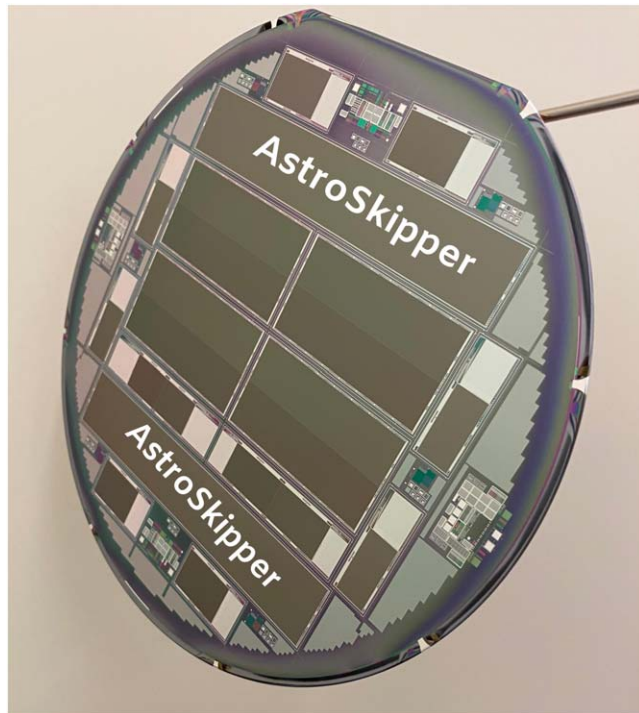


Figure 1. Silicon wafer (650–675 μm thick) containing 16 Skipper CCDs for different Fermilab R&D projects. The eight astronomy-grade Skipper CCDs are the 6k \times 1k format labeled as “AstroSkipper.” The AstroSkippers are Skipper CCDs that have been thinned to 250 μm , backside processed, and anti-reflective coated at the LBNL Microsystems Laboratory to produce detectors suitable for astronomical applications.

The AstroSkipper CCDs are p -channel devices fabricated on high resistivity ($>5 \text{ k}\Omega \text{ cm}$), n -type silicon. p -channel CCDs have demonstrated an improved hardness to radiation-induced CTI when compared to n -channel CCDs due to the dopants used to form the CCD channels (Gow et al. 2014, 2016; Wood et al. 2017). The p -channel nature of the Skipper CCD makes this technology attractive for space-based astronomical applications. Furthermore, high QE in the optical and near-infrared (O/NIR) makes these detectors candidates for ground- and space-based astronomical spectroscopy. To reach QE $> 80\%$ in the O/NIR, our eight AstroSkipper CCDs were treated with an anti-reflective (AR) coating at the LBNL Microsystems Laboratory. The AR coating was developed for the DESI detectors and consists of a 20 nm layer of indium tin oxide (ITO), 38 nm ZrO_2 , and 106 nm of SiO_2 . This three-layer AR coating resulted in substantial QE improvements at shorter wavelengths ($< 600 \text{ nm}$) than the two-layer ITO/ SiO_2 coating that was used for the DECam detectors (Bebek et al. 2017; Groom et al. 2017). This result is reproduced in QE measurements of the AstroSkippers (Section 7.6).

Each silicon wafer contains 16 Skipper CCDs (Figure 1) with different readout and size configurations. The AstroSkipper detectors to be used for SIFS are standard wide-format

Skipper CCDs ($6k \times 1k$, $15 \mu\text{m}$ pixels) with four amplifiers (Figure 1). The choice of detector format and pixel size was informed by the current SIFS focal plane; a mosaic of four $6k \times 1k$ Skipper CCD detectors will be used to cover the full $\sim 4k \times 4k$ pixel area of the current SIFS detector in order to preserve the optical configuration of the instrument. More detailed plans for the construction of the Skipper CCD SIFS focal plane prototype can be found in Villalpando et al. (2022).

2.2. Detector Packaging

The AstroSkipper detector packaging was performed at Fermilab. We designed a four-side-butable package (Villalpando et al. 2022) that is similar to DECam packages (Diehl et al. 2008). The AstroSkipper package has two main components: a flexible cable for carrying electrical signals to/from the CCD and a mechanical foot for mounting the CCD to the focal plane. The packaging process consists of attaching the flexible cable and CCD to a Si substrate with epoxy, wirebonding the CCD pads to the flexible cable, attaching the CCD and cable assembly to a gold-plated invar foot for focal plane mounting, and placing the packaged AstroSkipper within an aluminum carrier box for storage, transport, and laboratory testing (Figure 2). The carrier box is designed to mount directly to the cold-plate inside the testing vacuum dewar. A set of custom mechanical fixtures were developed to standardize and streamline the packaging process building upon experience from packaging DECam and DESI detectors (Flaughner et al. 2015; Villalpando et al. 2022).

3. AstroSkipper Testing Procedures and Infrastructure

We have packaged, tested, and optimized eight AstroSkipper CCDs, four of which will be used for the construction of the Skipper CCD focal plane prototype for SIFS. Two of the AstroSkippers were found to have cosmetic and photon-counting performance issues in at least one amplifier, leaving six high-quality AstroSkippers suitable for the SIFS focal plane. This corresponds to a detector yield of 75% and a Skipper amplifier yield of 97% (i.e., we define a working amplifier as an amplifier that can register a charge measurement and can count photons).

First, we optimize the AstroSkipper readout time (see Section 4) by minimizing the pixel integration window and the horizontal sequence times to reach a total pixel time of $\sim 40 \mu\text{s pixel}^{-1}$ for a single-sample. Subsequent characterization tests are performed with this optimized readout time. We developed a streamlined procedure for testing detectors: we collect single and multi-sample bias and dark frames, flat fields at different illumination levels, and ^{55}Fe X-ray data. Based on the results of each test, we determined whether each detector passed the requirements for inclusion in the SIFS focal plane. We refer to the performance metrics used to evaluate the DESI



Figure 2. Fully packaged AstroSkipper housed in a carrier box. The package is a four-side-butable pedestal package similar to DECam packages (Diehl et al. 2008). The detector and flexible cable assembly is attached to a gold-plated invar foot that serves as the rigid structure for mounting the AstroSkipper to the focal plane. For lab testing, the detector remains inside the carrier box. The box is mounted to the cold-plate in the dewar, and the lid of the box is removed to expose the detector for characterization tests using light.

red and NIR CCDs tested at Fermilab to assess the AstroSkippers (Bonati et al. 2020); these metrics are also similar to DECam performance requirements (Diehl et al. 2008).

3.1. Testing Equipment

The AstroSkipper CCDs undergo testing employing the optical setup shown in Figure 3. Characterization of DECam and DESI detectors utilized a similar optical setup (Diehl et al. 2008; Bonati et al. 2020). This setup is located in a “dark room” in order to reduce external light entering the testing station. A single AstroSkipper CCD is housed in a thermally controlled vacuum dewar with a fused silica window for illumination purposes. The AstroSkipper carrier box (Figure 2) attaches to an aluminum plate that is screwed to a copper cold finger inside the vacuum dewar. The system is cooled by a closed-cycle cryocooler to an operating temperature of 140K,

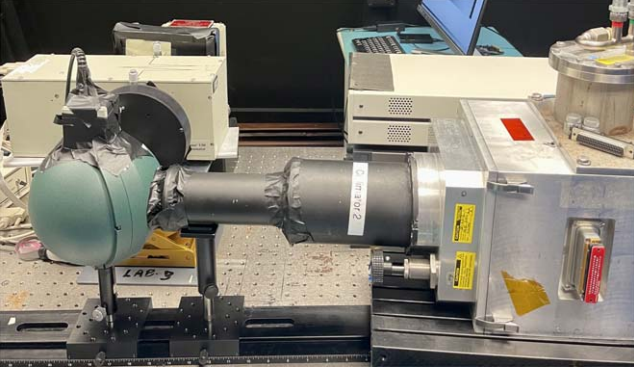


Figure 3. Skipper CCD testing station. From the right, closed-cycle vacuum dewar (vacuum cube), collimator, integrating sphere (photodiode mounted on top), shutter, monochromator, filter wheel, quartz tungsten halogen lamp. Light enters the vacuum dewar through a fused-silica window. The Skipper CCD is mounted on a cold aluminum plate that faces the window.

which is maintained by a LakeShore temperature controller. A standard set of optical devices consisting of a quartz tungsten halogen lamp, motorized filter wheel, monochromator, shutter, and integrating sphere are used to provide uniform illumination of the AstroSkipper surface in the targeted wavelength. Light intensity is measured independently by a National Institute of Standards and Technology (NIST)-traceable Oriel photodiode mounted on the integrating sphere. This first photodiode, in conjugation with a second Thorlabs NIST-traceable photodiode mounted at the position of the CCD, allows us to calibrate the photon flux for absolute QE measurements. The shutter, filter wheel, and monochromator are controlled using a serial-to-Ethernet interface.

3.2. Readout Electronics and Data Acquisition

The readout chain consists of a second-stage flex cable, an output dewar board, which provides the pre-amplification stage, and a low-threshold acquisition (LTA) board. The flexible cable has two high performance LSJ689-SOT-23, p -channel junction-gate field-effect transistors, providing ultra-low noise (~ 2.0 nV/ $\sqrt{\text{Hz}}$), four 20 k Ω resistors, and a 51-pin Omnetics connector. The LTA readout board was designed at Fermilab as an optimized readout system for p -channel, thick, high resistivity Skipper CCDs (Cancelo et al. 2021). The LTA’s flexibility allows the operation of Skipper CCDs to be optimized for different applications (e.g., DM direct detection and astronomy). The LTA is a single-printed circuit board hosting four video amplifiers for readout, plus CCD biases and clock control. The LTA is controlled by a Xilinx Atrix XC7A200T FPGA, which sets programmable bias and clock voltages, video acquisition, telemetry, and data transfer from the board to the PC. The user can communicate with the LTA via terminal commands to perform board configuration, readout and telemetry requests, and sequencer uploading. The data

acquisition comes in the form of images in FITS format for subsequent analysis.

4. AstroSkipper Readout Time Optimization

The Skipper CCD’s ability to achieve ultra-low noise comes at the cost of the readout time. When taking a large number of non-destructive measurements of the charge in each pixel, the readout timescales are approximately $t_{\text{readout}} \propto N_{\text{samp}} \propto 1/\sigma_N^2$. In applications that require ultra-low noise, data taking can take several hours (e.g., Barak et al. 2020). In astronomical applications, the readout and exposure time need to be optimized to maximize the signal-to-noise of a faint astronomical source in a fixed observation time (Drlica-Wagner et al. 2020). Therefore, it is a priority to reduce the AstroSkipper’s readout time while maintaining relatively low single-sample noise performance. Readout time optimization is independent of the detector’s processing (e.g., backside thinning), and we expect that time performance optimizations can be applied to other Skipper CCDs intended for astronomy or applications that require fast readout.

The total readout time for a single amplifier, in a given sequence, i.e., the clocking sequence used to move the charge to the Skipper CCD’s sense node, is as follows

$$t_{\text{readout}} = N_{\text{ROW}}[(t_{\text{pixel}}N_{\text{samp}} + t_{\text{H}})N_{\text{COL}} + t_{\text{V}}] \quad (2)$$

where t_{pixel} is the pixel integration time window including both the pedestal and signal components (Figure 4; right panel), N_{samp} is the number of non-destructive measurements, t_{H} is the time required for the horizontal sequence, i.e., serial register clocking during the charge transfer to the summing well, t_{V} is the time for the vertical clocking, i.e., the time to move the charge toward the serial register, N_{ROW} and N_{COL} define the CCD dimensions (CCD rows and columns). From Equation (2), we can see that t_{pixel} and t_{H} have the greatest contribution to the total readout time (t_{readout}); therefore, we attempt to optimize these two times in the sequence. Let us consider the charge in one pixel that is transferred by the horizontal clocks from the serial register to the summing well. After that, the sense node is reset via the reset gate, setting a reference value for the charge measurement known as pedestal (PED) level. The charge is then transferred to the floating gate (sense node), passing through the output gate where another measurement is performed; this value is known as the signal level (SIG). The pixel value is obtained by applying CDS over the analog-to-digital converter output samples, computing the difference between the signal and the pedestal levels. The charge packet is either discarded via the dump gate or returned to the summing well using the output gate, and the process is repeated a total of N_{samp} times (Lapi et al. 2022). Figure 4 depicts this process of charge transferring in the Skipper CCD output stage. The time for computing the pixel value, i.e., the

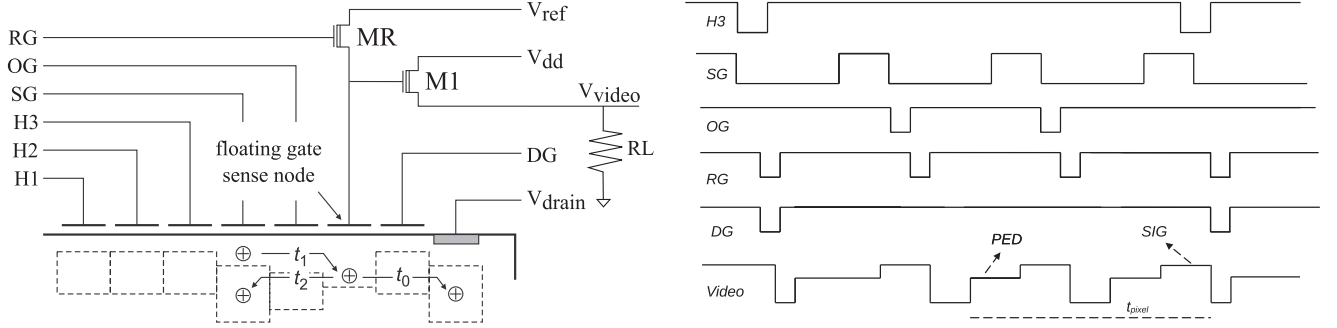


Figure 4. Left: simplified diagram of the Skipper CCD output stage Reproduced from [Tiffenberg et al. 2017], CC BY 4.0. Right: charge transfer diagram for the Skipper CCD output stage. This diagram is adapted from Figure 5 in Fernández Moroni et al. (2012). Clock phases are defined in Section 4.

pixel integration window time (t_{pixel}) is given by

$$t_{\text{pixel}} = t_{\text{wt1}} + t_{\text{PED}} + t_{\text{wt2}} + t_{\text{SIG}} \quad (3)$$

where t_{wt1} and t_{wt2} represent the wait times in the pedestal and signal integration periods; these are resting times with samples that are not being integrated either in the pedestal ($t_{\text{wt1}} + t_{\text{PED}}$) or signal ($t_{\text{wt2}} + t_{\text{SIG}}$) integration intervals. The addition of these waiting times improves noise characteristics as the system does not integrate noise-dominated samples from the transients in the video signal after the sense node is reset.

Optimizing the readout time consists of fixing the integration window in the sequence, and varying t_{PED} and t_{SIG} for each integration window instance with the condition that $t_{\text{PED}} = t_{\text{SIG}}$ for a series of t_{wt1} and t_{wt2} . For each configuration, i.e., an instance of a fixed integration window, we measure the readout noise. To perform the readout noise scan, we take single-sample images without integrating the charge (charge-less readout), i.e., we clock the charge in the opposite direction to the amplifiers, enabling measurements of the noise properties of the system, and ignoring contributions due to charge accumulation. We find that t_{wt1} can be set to $0 \mu\text{s}$ while t_{wt2} can be set to values $0 \mu\text{s} < t_{\text{wt2}} < 2 \mu\text{s}$. Figure 5 (top panel) shows the optimal readout noise for different integration window time instances for one AstroSkipper. We find that it is possible to shorten the integration window to $20 \mu\text{s}$ while maintaining a readout noise of $\sigma_1 < 4.3 \text{ e}^- \text{ rms pixel}^{-1}$ for the six AstroSkippers. This is a factor of two reduction in the integration time compared to the original configuration used for the SENSEI DM direct detection experiment (Crisler et al. 2018). In Figure 5 (bottom panel), we calculate the readout speed, using Equation (2), as a function of the integration window time while varying N_{samp} to reach photon-counting resolution (e.g., $\sigma_N \sim 0.18 \text{ e}^- \text{ rms pixel}^{-1}$). The optimal integration window time is $t_{\text{pixel}} \sim 20 \mu\text{s}$ for a readout speed of $\sim 330 \text{ pixel s}^{-1}$ for $N_{\text{samp}} = 400$. Furthermore, we reduced t_{H} from 100 to $20 \mu\text{s}$, the limit set by the time constant of the horizontal clocks RC filters for reducing CIC (Section 6). These time optimization improvements result in a total pixel readout of $\sim 40 \mu\text{s pixel}^{-1}$ for one sample (i.e., $25 \text{ kpixels s}^{-1}$ per

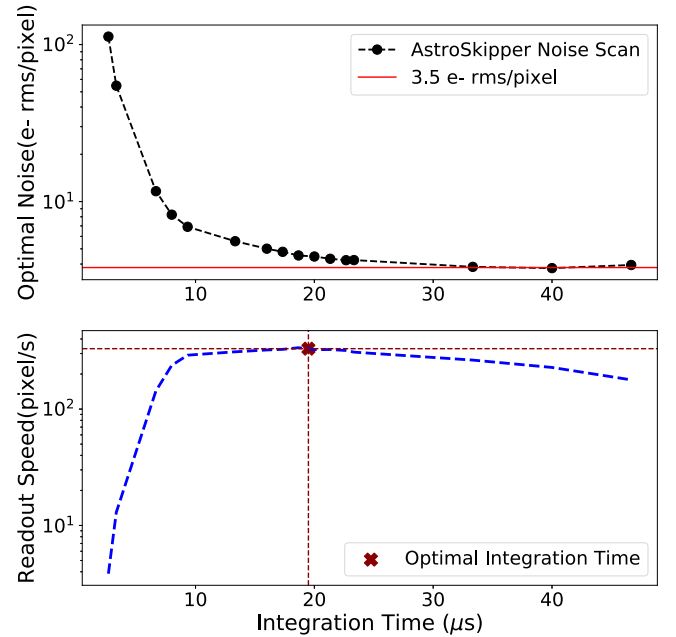


Figure 5. Top: measured single-sample readout noise vs. CDS integration window time for the AstroSkipper. For each fixed integration window instance, we calculate the optimal noise for different t_{wt2} , t_{PED} , and t_{SIG} with $t_{\text{wt1}} = 0 \mu\text{s}$. We note that the curve approaches the noise floor ($3.5 \text{ e}^- \text{ rms pixel}^{-1}$) at $\sim 20 \mu\text{s}$ with a readout noise $\sigma_1 \sim 4.3 \text{ e}^- \text{ rms pixel}^{-1}$. Bottom: readout speed in pixel s^{-1} as a function of the integration time while varying N_{samp} to achieve photon-counting resolution ($\sigma_N \sim 0.18 \text{ e}^- \text{ rms pixel}^{-1}$). The optimal integration window time is $\sim 20 \mu\text{s}$ for a readout speed of $\sim 330 \text{ pixel s}^{-1}$.

amplifier) or ~ 1.28 minutes to read the whole detector with $N_{\text{samp}} = 1$. This is compared to $\sim 200 \mu\text{s pixel}^{-1}$ for a single amplifier and pixel sample commonly used for DM experiments (Crisler et al. 2018).

4.1. Skipper CCD Regions of Interest Time Optimization

Despite the timing optimization described in the previous section, it is clear from Figure 5 that it would still take several

hours to achieve photon-counting resolution over the entire detector. These long readout times are unacceptable for astronomical applications. For astronomical observations, there is a minimum at which the signal-to-noise improvements due to reducing readout noise is overcome by the lost exposure time during long readout times, i.e., time used for readout could alternatively be used to collect more signal. Therefore, it is a priority to explore readout noise configurations for a particular application and optimize the AstroSkipper parameters (e.g., N_{samp}) to reach the desired noise performance in the least amount of time.

Drlica-Wagner et al. (2020) calculated the optimal readout noise for Ly α observations with the DESI multi-object spectrograph, considering two scenarios: maximize the signal-to-noise at a fixed observation time or alternatively minimize the observation time at a fixed signal-to-noise (see Figure 1 in Drlica-Wagner et al. 2020). In both instances, an optimum was found at $\sigma_N \sim 0.5 \text{ e}^- \text{ rms pixel}^{-1}$, assuming that only 5% of the detector pixels need to be read with the improved signal-to-noise. It would take ~ 40 minutes to achieve $\sim 0.5 \text{ e}^- \text{ rms pixel}^{-1}$ in all detector pixels, and we attempt to shorten these long readout times by exploiting the region of interest (ROI) capability of the Skipper CCD (Drlica-Wagner et al. 2020; Chierchie et al. 2021). We can define a geometrical area on the Skipper CCD (e.g., 5% of the detector area) that is read with multiple samples. For our implementation, this ROI will correspond to a specific wavelength range produced by the SIFS spectrograph. The ROI can be read with reduced noise (e.g., $0.5 \text{ e}^- \text{ rms pixel}^{-1}$) while the rest of the detector is read once with single-sample noise.

We use each integration window instance time and single-sample readout noise (top panel in Figure 5) to find the optimal configuration of pixel integration time and number of samples (N_{samp}) to reach $0.5 \text{ e}^- \text{ rms pixel}^{-1}$ in 5% of the detector area and minimize the readout time per frame. From Equation (1), which describes the relationship between readout noise and the number of non-destructive read samples (N_{samp}), one sees that $N_{\text{samp}} = \left(\frac{\sigma_1}{\sigma_N}\right)^2$ where $\sigma_N = 0.5 \text{ e}^- \text{ rms pixel}^{-1}$ and σ_1 is the optimal single-sample readout noise in the top panel of Figure 5. For each N_{samp} and integration time (t_{pixel}), we use Equation (2) to calculate the total readout time. Figure 6 shows the optimal pixel integration time ($\sim 20 \mu\text{s}$) that minimizes the total readout time for a frame with $\sigma_N = 0.5 \text{ e}^- \text{ rms pixel}^{-1}$ in 5% of the pixels. We can then calculate the total readout time for a full frame where 5% of the detector is readout with $0.5 \text{ e}^- \text{ rms pixel}^{-1}$ and the remaining 95% with single-sample readout noise, which comes out to $t_{\text{readout}} \sim 3.6$ minutes.

5. Skipper CCD Enabled Characterization Tests

The ultra-low noise capability of the Skipper CCD enables several interesting measurements of detector performance in the photon-counting regime. For instance, the capability to

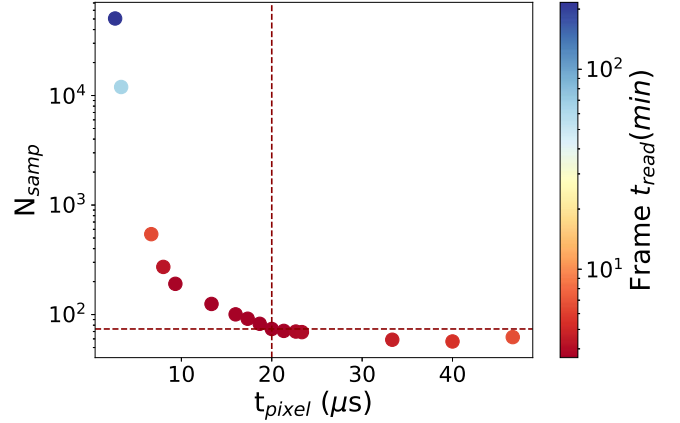


Figure 6. Optimization of the integration time (t_{pixel}) to achieve a noise of $0.5 \text{ e}^- \text{ rms pixel}^{-1}$ in 5% of the detector area and minimize the total readout time per frame. The optimal integration value is found to be $\sim 20 \mu\text{s}$ which allows the full frame to be read in ~ 3.6 minutes.

resolve individual electrons, allows for a precise measurement of the detector’s gain, the conversion between Analog-to-Digital Units (ADU) and electrons. Furthermore, resolving individual electrons allows for nonlinearity measurements at low signals, which can be challenging to perform with conventional scientific CCDs.

5.1. Readout Noise Characteristics and Photon-counting

The readout noise of a Skipper CCD is tunable through multiple non-destructive measurements of the charge in each pixel. For uncorrelated Gaussian noise, the effective readout noise distribution from averaging N_{samp} non-destructive measurements will scale as $\sigma_N \propto 1/\sqrt{N_{\text{samp}}}$ (Equation (1)). We note that the readout noise is a combination of intrinsic electronic noise and external noise sources, which are dependent on specific testing stations and factors such as electronic grounding. We measure the readout noise from processed images, i.e., overscan subtracted images. To account for non-uniformities in the overscan pedestal level, the overscan subtraction algorithm fits the pixel distribution of each row in the overscan region with a multi-Gaussian model and subtracts the mean of the 0 e^- peak to that row. Similarly to Drlica-Wagner et al. (2020) and Villalpando et al. (2022), the readout noise we measure is given by the standard deviation of the 0 e^- peak. Figure 7 shows a 600×3200 pixel image where the overscan region starts at pixel 3080. The middle panel plots the structure of the pedestal in the overscan and activated regions in a single-sample image. We observe a slowly decaying transient that is correlated with row number; this same behavior is present in both multi- and single-sample images. The pedestal subtraction algorithm is able to correct for this row-dependent variation as observed in the bottom panel (pedestal subtracted traces).

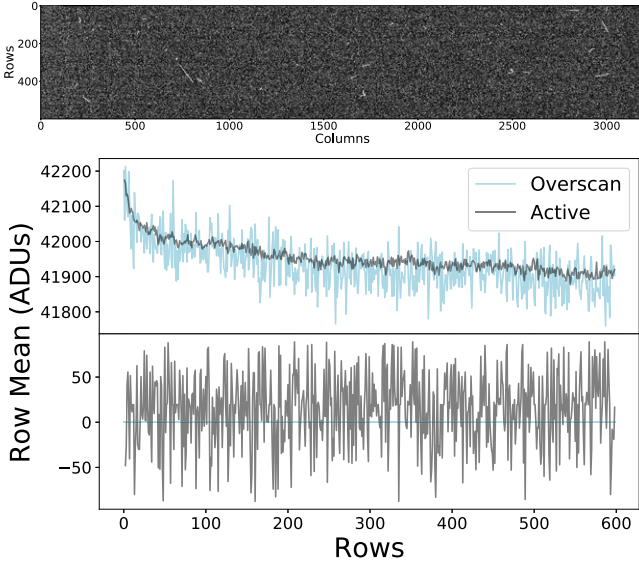


Figure 7. Top: single-sample image from one AstroSkipper quadrant (600×3200 pixels) with overscan region starting at the 3080 pixel. Middle: average pixel value calculated per row in the overscan (blue) and active (black) regions of the detector. A large scale transient correlated with row number can be seen. Bottom: same as the middle panel, but after row-by-row overscan pedestal subtraction. The algorithm corrects the slowly decaying transient associated with row number.

We measure the readout noise for all 32 AstroSkipper amplifiers (eight detectors with four amplifiers per detector) and find values ranging from $3.5 e^- \text{ rms pixel}^{-1}$ to $5 e^- \text{ rms pixel}^{-1}$; the six astronomy-grade detectors maintain a readout noise $< 4.3 e^- \text{ rms pixel}^{-1}$ for all 24 amplifiers. In Figure 8, we show an example of photon-counting (left) and noise reduction (right) achieved by one of the AstroSkippers with 400 samples per pixel. To simplify the calculation of the readout noise as a function of N_{samp} , we again implement the charge-less readout without integration charge to measure only the noise characteristics of the system. The measured noise varies from the expected Gaussian noise model (Equation (1)) by $\lesssim 20\%$ for $N_{\text{samp}} < 10$ and 10% for $N_{\text{samp}} > 150$ (Figure 8, right). We note that the greatest contribution to variations in the noise model comes from instabilities in the first few samples. Similar behavior was seen in early testing of Skipper CCDs (Fernández Moroni et al. 2012), where it was postulated that variations in the readout noise at low N_{samp} are produced by residual low-frequency noise, and fluctuations at large samples might be due to external or unidentified sources of noise coupling to the readout electronics. At low sample numbers, fluctuations in the clock-induced transients can dominate the noise behavior; however these transients settle as N_{samp} increases. For instance, if the averaging starts from $N_{\text{samp}} = 5$, the variation in the noise measurements with respect to the Gaussian noise model reduces to $< 3\%$ for all sample

numbers. Figure 9 shows the single (σ_1) and multi-sample (σ_{400}) noise performance for each amplifier and detector.

Since each peak in the pixel distribution histogram (Figure 8) differs from its neighbor by a single electron, we can obtain a direct measurement of the detector’s gain by calculating the difference between adjacent electron peaks, i.e., the gain would be given by $\Delta_{i,i+1}$ where $\Delta_{i,i+1} = \mu_{i+1} - \mu_i$ is the difference between the means of the Gaussian fits to the i and $i + 1$ adjacent electron peaks. Figure 10 shows gain measurements per amplifier from the six AstroSkippers; gain measurements depend on resolving the electron peaks in each amplifier, and applying the method described above. We use the $0 e^-$, $1 e^-$, and $2 e^-$ electron peaks ($\Delta_{0,1}$, $\Delta_{1,2}$) and take the average between both $\Delta_{i,i+1}$ to calculate these gain values for all amplifiers. We measure gain values ranging from $\sim 123 \text{ ADU}/e^-$ to $\sim 143 \text{ ADU}/e^-$ (left) for amplifiers on all six of the astronomy-grade AstroSkippers with average variations of $< 6\%$ between gain values from all amplifiers. We do not see any clear correlation between amplifier gain and amplifier noise.

5.2. Nonlinearity

The AstroSkipper’s large dynamic range and ability to count individual charge carriers enables a unique avenue to measure linearity at both low and high illumination levels. At high illumination levels, we follow a conventional approach to measure nonlinearity by increasing the exposure times. We study a wide range of images taken with high illumination levels from $1500 e^- \text{ pixel}^{-1}$ to values near saturation. The data taking procedure consists of taking ~ 20 flat-fields with increasing illumination; we perform bias subtraction and sigma clipping to eliminate cosmic rays on each frame. We calculate nonlinearity following the procedure implemented by Bonati et al. (2020) to measure the nonlinearity of the DESI detectors. To compute the nonlinearity over our data set of 20 flat-field images, we implement a least-squares fit to minimize the sum of the squares of the error $E(\alpha, \beta) = \sum_{n=1}^{20} (y_n - (\alpha x_n + \beta))^2$. Here n indexes over the images, y_n is the mean of the pixel values for image n , x_n is the exposure time for image n , and α and β are the parameters of the linear fit. We find the values of α and β that minimize $E(\alpha, \beta)$, i.e., $\partial E / \partial \alpha = 0$, $\partial E / \partial \beta = 0$. The nonlinearity factor is then given by the mean value of the square-root of the residuals $E(\alpha, \beta)$. We find nonlinearity values $< 0.05\%$ for all of the amplifiers in the six AstroSkipper CCDs.

In conventional CCDs, low-signal-level nonlinearities are poorly understood since these CCDs lack the precision to quantize charge in the single-electron regime. In contrast, Skipper CCDs can quantify nonlinearities for all electron occupancies, i.e., they can resolve electron peaks for the full range. For instance, in Bernstein et al. (2017) nonlinearity measurements for a subset of DECam devices show poorly understood behavior at low illumination levels (few tens of electrons). The AstroSkipper allows us to precisely characterize

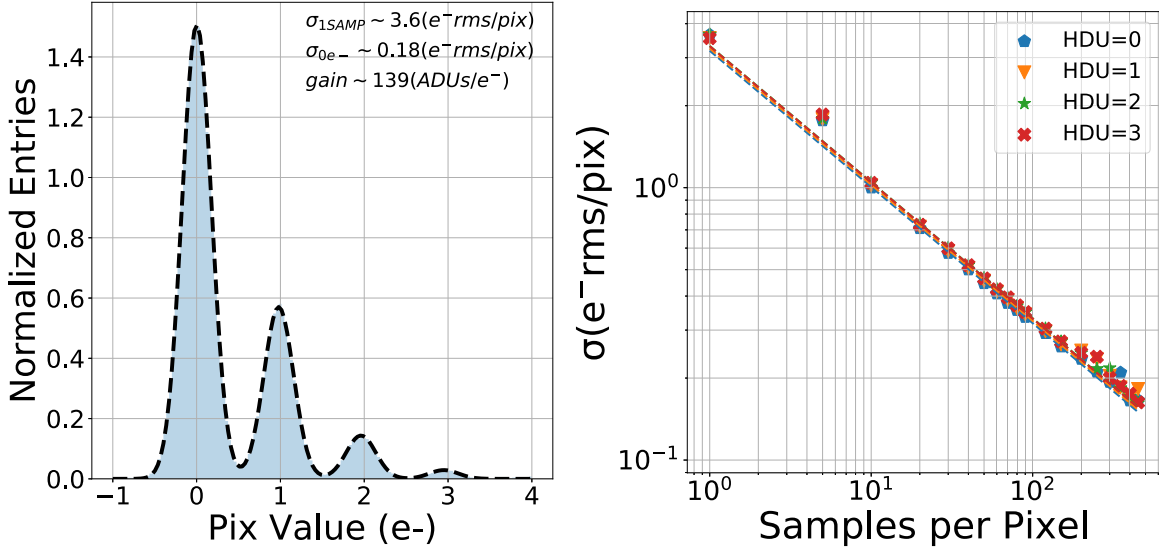


Figure 8. Readout noise characteristics and photon-counting for one of the AstroSkipper CCDs. Left: histogram of the pixel values for one amplifier calculated from the average of 400 non-destructive measurements (samples) per pixel (cyan histogram). The low noise ($\sigma_{0e^-} \sim 0.18 e^- rms pixel^{-1}$) achieved after $N_{samp} = 400$ resolves single electrons/photons. We see photon-counting capabilities in all amplifiers from the six AstroSkippers. We fit the distribution of pixel values with a multi-Gaussian model. The gain of the detector can be directly calculated from the difference between the mean values in ADUs of adjacent electron peaks. Right: readout noise for four amplifiers as a function of the number of non-destructive measurements of each pixel (N_{samp}). The measurements deviate from the expectation from Equation (1) (dashed line) by as much as 20% and 10% for $N_{samp} < 10$ and $N_{samp} > 150$, respectively.

nonlinearity in this regime of a few tens of electrons following a procedure similar to the one described in Rodrigues et al. (2021). In the photon-counting regime, one can probe nonlinearities by measuring variations in the relationship between the number of electrons in each pixel and the signal readout value in ADUs (i.e., the gain).

We take several flat-field images with 400 samples per pixel to reach single-electron resolution with $\sigma_{400} \sim 0.18 e^- rms pixel^{-1}$. Images are taken with increasing exposure time where the set of images produce different overlapping Poisson distributions with an increasing mean number of electrons (Rodrigues et al. 2021). We resolved up to $50 e^-$, i.e., it is possible to count individual peaks up to the 50th electron peak in the set of images. To perform the nonlinearity measurement, we fit each electron peak with a Gaussian and compute the gain from each peak by dividing the mean value of the difference between the electron peak and the $0 e^-$ peak in ADU by the peak's assigned electron number, $(\mu_i - \mu_0)/i$. For example the gain calculated from the 10th electron peak would be given by $(\mu_{10} - \mu_0)/10 e^-$ where $(\mu_{10} - \mu_0)$ is the difference (in ADU) between the means of Gaussian fits to the $0 e^-$ and $10 e^-$ peaks and $10 e^-$ is the assigned number of electrons for that peak. We note that this method for charge quantization results in increased variability when computing gain values at low electron counts and diminishes for higher electron counts since variations in the mean get divided by the amount of charge. If we instead calculate the gain from the peak-to-peak separation, i.e., $\mu_{i+1} - \mu_i$, we find a consistent gain with a

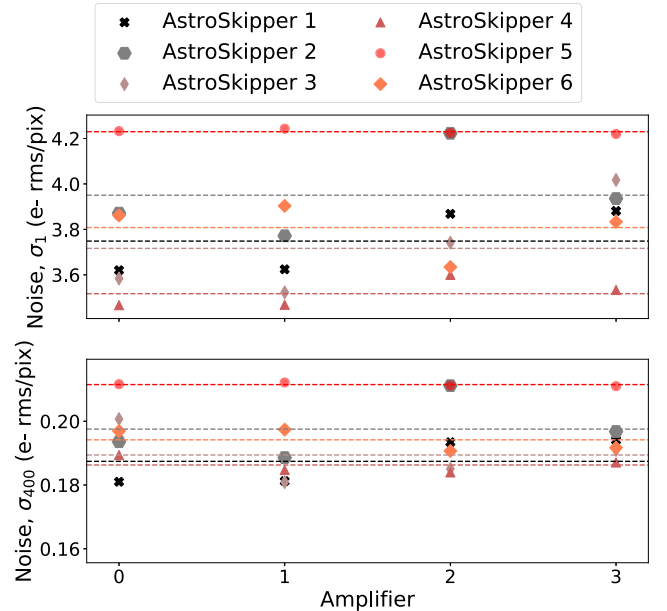


Figure 9. Variation in the noise characteristics of the four amplifiers in the six selected Skipper CCDs. Top: single-sample readout noise values for each amplifier. Bottom: noise performance per amplifier after taking 400 non-destructive measurements of the charge in each pixel. Dotted lines are the average readout noise for a given amplifier.

scatter of $<4\%$ between individual electron peaks (though we note that adjacent points are highly correlated).

Figure 11 (top) shows peak-to-peak gain calculations and as expected, we observe a greater spread between gain values. The

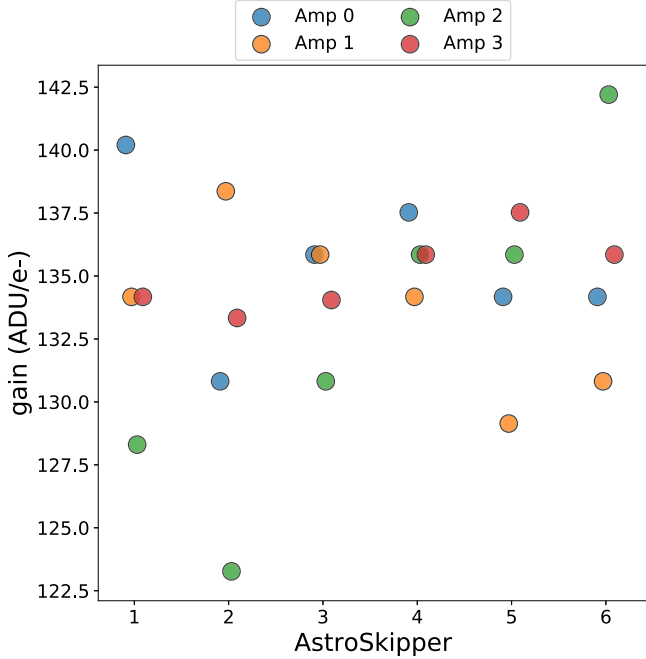


Figure 10. Gain measurements for all amplifiers for the six AstroSkipper CCDs. Gain calculated using separation between electron peaks in each detector’s amplifier for all six AstroSkippers. We see variations of $<6\%$ on average between gain values in all amplifiers; amplifiers 1 and 2 show the largest variation on average for all detectors.

bottom panel shows a low-signal nonlinearity measurement for one of the AstroSkippers where we represent the nonlinearity as the deviation from the unity of the ratio between the gain calculated as $(\mu_i - \mu_0)/i$ and the fixed, conventional gain value measured from the slope of the variance versus the signal in the PTC (Section 7.3). We find nonlinearity values that are $<1.5\%$ at this low-signal regime of a few tens of electrons which agrees with values reported in Rodrigues et al. (2021) ($<2.0\%$). Furthermore, this method for calculating nonlinearity also shows the agreement between PTC and charge quantization gain calculations. Similar to Drlica-Wagner et al. (2020), we find that the gain measurements from the two methods agree within $\sim 1\%$.

6. Clock-induced Charge and Voltage Optimization

CIC can be an appreciable background for measurements in the single-photon/single-electron regime (e.g., Janesick 2001; Tulloch & Dhillon 2011). The SENSEI direct DM detection experiment measures a CIC rate of $\sim 1.52 \times 10^{-4} e^- \text{ pixel}^{-1} \text{ frame}^{-1}$ with a low-voltage configuration for a Skipper CCD similar in pixel and readout configuration to the AstroSkipper (Barak et al. 2020). Implementing this low-voltage configuration under the AstroSkipper testing conditions, we measure an average electron rate of $\sim 1.45 \times 10^{-3} e^- \text{ pixel}^{-1} \text{ frame}^{-1}$, which sets an upper limit on the CIC contribution. The full-well capacity in this configuration is

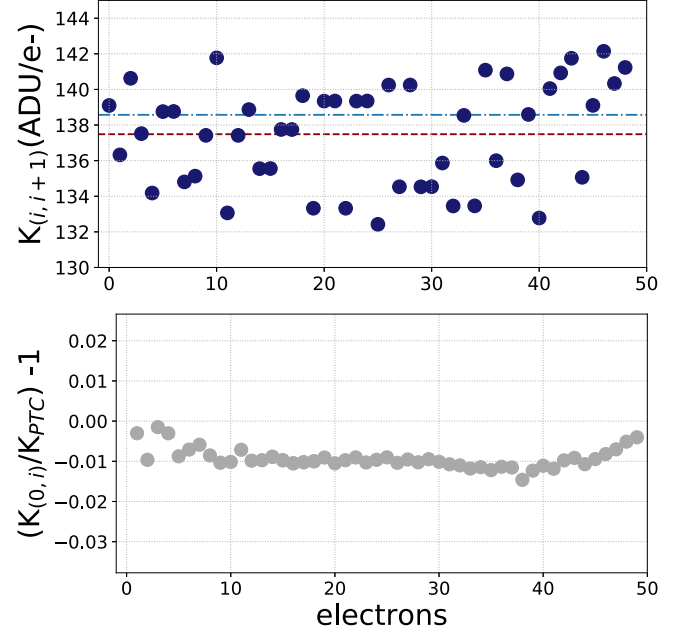


Figure 11. Top: gain values calculated from peak-to-peak separation of individual electron peaks, i.e., $\mu_{i+1} - \mu_i$. The average gain is $\sim 139 \text{ ADU}/e^-$ (red dashed line) with a scatter about this mean of $<4\%$. The blue dash-dotted line represents the gain value estimated from the slope of the signal variance vs. the signal mean in the PTC. Bottom: ratio between the gain measured from the difference between the 0th and i th electron peak, i.e., $(\mu_i - \mu_0)/i$, and the constant gain value from the PTC. We observe a $\sim 1\%$ agreement between the two methods for determining the gain and $<1\%$ variations in the gain as measured from the electron peak.

$\sim 900 e^-$. Considering the AstroSkipper application, it is important to study the tradeoff between CIC and full-well capacity. Achieving full-well capacities suitable for the anticipated signal levels from calibration and data products for SIFS requires using higher voltages than SENSEI; however, higher voltage swings, specially in the serial register, increase CIC. Thus, CIC can become an important background for astronomical measurements with the AstroSkipper. Therefore, we study CIC production in the AstroSkipper and optimize voltages to reach high full-well capacities for the SIFS application while minimizing CIC and maintaining photon-counting capabilities.

6.1. AstroSkipper CIC

CIC is generated during the clocking sequence when inverting clocks between the high and low-voltage states. When switching the clock to the non-inverted state, holes that become trapped at the Si–SiO₂ interface during clock inversion are accelerated with sufficient energy to create electron–hole pairs through impact ionization (Janesick 2001). Released electrons are then collected in the summing well and contribute to the overall readout signal. In conventional CCDs, where the noise floor can be $>5 e^- \text{ rms pixel}^{-1}$, CIC is not apparent, i.e.,

the charge produced by CIC can be characterized as shot noise with a contribution of $N_{\text{CIC}} = \sqrt{\mu_{\text{CIC}}}$ where μ_{CIC} is the average CIC in electrons (Janesick 2001) and for $\mu_{\text{CIC}} = 3 \text{ e}^- \text{ pixel}^{-1} \text{ frame}^{-1}$ (typical value observed with an AstroSkipper at high operating voltages) the CIC noise contribution of $\sim 1.7 \text{ e}^- \text{ rms pixel}^{-1}$ would be lower than the noise floor and thus undetectable. However, for ultra-low-noise detectors operating in the photon-counting regime, CIC is an important source of background for observations of faint sources (e.g., Kyne et al. 2016).

We focus on optimizing the CIC with respect to the horizontal clock swings since we find that CIC produced in the activated area is negligible compared to CIC generated in the serial register. First, we build a statistical model to predict the electron event rate from CIC as a function of the horizontal clock voltage swings. Since CIC can be characterized as shot noise, we assume it obeys Poisson statistics and therefore the expected CIC electron rate is given by the Poisson probability mass function (PMF)

$$P(X = k) = \frac{\exp(-\mu)\mu^k}{k!} \quad (4)$$

where $P(X = k)$ gives the probability of observing k events (CIC electron rate) in a given interval, and μ is the average rate of CIC electron events for the full readout sequence. Furthermore, we assume that the average rate of CIC electron events (μ) can be modeled with an exponential, which describes the growth of CIC electron events with respect to the horizontal clock swings,

$$\mu = a \exp(b\Delta H) + c. \quad (5)$$

Here ΔH is the horizontal clock voltage swing and a , b , and c are fit parameters. To calculate the best fit for μ , we take several dark frames with increasing ΔH and electron resolution ($N_{\text{samp}} = 400$, $\sigma_{400} \sim 0.18 \text{ e}^- \text{ rms pixel}^{-1}$) in order to resolve single electron rates from CIC. To get μ , we fit a single Gaussian model to the pixel distribution, containing CIC electron rate peaks, and subtract the background, which is calculated with the low-voltage configuration that generates minimum CIC (i.e., $\lesssim 1.45 \times 10^{-3} \text{ e}^- \text{ pixel}^{-1} \text{ frame}^{-1}$). We fit an exponential model to find the values of a , b , and c in Equation (5).

The number of transfers in the serial register is closely related to CIC (Janesick 2001); the probability of generating a CIC electron event increases as the pixel is clocked more times in the serial register. To investigate how the number of transfers (NT) affect our probabilistic model, we calculate CIC for one quadrant of the smaller format (1248×724 , $15 \mu\text{m} \times 15 \mu\text{m}$ pixels) Skipper CCD characterized in Drlica-Wagner et al. (2020). We use the voltage configurations tested in the AstroSkipper and repeat the same data taking procedure, i.e., dark frames ($\sigma_N \sim 0.18 \text{ e}^- \text{ rms pixel}^{-1}$). We consider CIC_{1i} and CIC_{2i} : the average CIC electron rate per pixel per frame

from the smaller Skipper CCD and the AstroSkipper, respectively. Assuming a linear relationship between both data sets (informed by CIC production in Janesick 2001), the linear regression model is

$$\text{CIC}_{2i} = \beta_0 + \beta_1 \cdot \text{CIC}_{1i} + \epsilon_i \quad (6)$$

where β_0 is the rate of CIC generation, related to the relative NT between both detectors, β_1 is the intercept, and ϵ_i is the error term associated with the i th observation in CIC_{2i} . We perform a linear regression to find β_0 and β_1 , minimizing the sum of squared residuals, $\sum \epsilon_i^2$. Figure 12 (left) shows the linear relationship between CIC_{1i} and CIC_{2i} with $\beta_0 \sim 7.1$ (a factor of 7 increase in CIC for the AstroSkipper with 3200 transfers compared to 450 transfers for the smaller Skipper CCD).

Figure 12 (right) shows the simulated CIC rate from the statistical model, i.e., random draws from the Poisson PMF, and the measured data; we see better than $\sim 10\%$ agreement, for $\Delta H > 7.5 \text{ V}$, between the model and the measured data. We note that this model assumes a fixed horizontal clock filtering solution, and horizontal clock width. In future work, we will generalize the statistical model formalism to include the effect from varying clock pulse width, i.e., the time the clock spends in the non-inverted state immediately after inversion, and the CIC reduction from different clock shaping solutions (Janesick 2001; Daigle et al. 2009, 2010).

Because CIC is closely linked to horizontal clock voltage swing (ΔH) and the full-well capacity is also dependent on ΔH , we must optimize CIC and full-well capacity for the expected signal levels in the application. To mitigate CIC, we have implemented a simple filtering solution consisting of a first-order low-pass filter with a time constant $\tau = 5.1 \mu\text{s}$ placed between the pre-amplification stage and the LTA. This allows for a factor of ~ 2 reduction in CIC electron events for $\Delta H > 9 \text{ V}$, which yields the highest full-well capacity.

6.2. Voltage Optimization

Previous Skipper CCD operational parameters, such as clock voltage values, were primarily optimized for reducing CIC for DM direct detection and rare particle searches where operational processes that can produce a few electron events severely reduce sensitivity to rare events (Tiffenberg et al. 2017; Crisler et al. 2018; Barak et al. 2022). However, the small voltages used for these rare particle searches limit the dynamic range of the Skipper CCD, which can be problematic for most astronomical applications. We perform a voltage optimization for the AstroSkipper in order to increase the dynamic range while maintaining low CIC, stable readout noise, and photon-counting capabilities.

The full-well capacity is derived from the PTC. Due to the CIC and full-well dependence on the horizontal clocks swing voltage, we optimize ΔH for reducing CIC while maintaining a

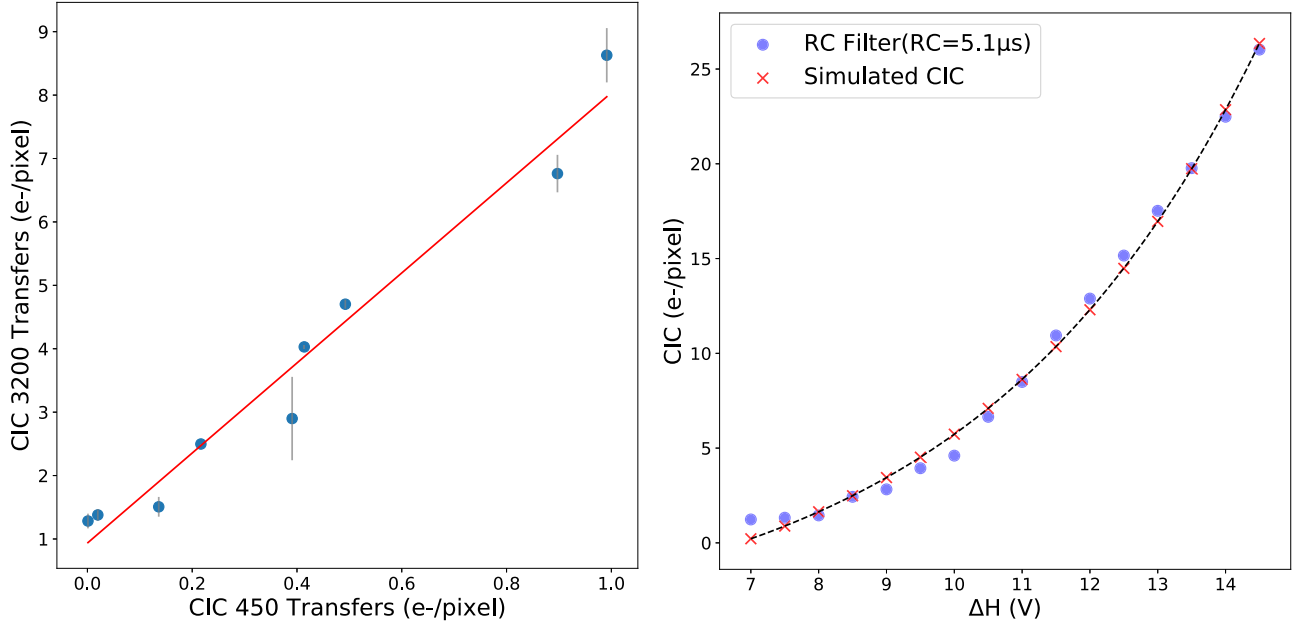


Figure 12. Modeling CIC generation. Left: linear relationship between CIC and number of transfers in the serial register. Each data point corresponds to a different horizontal clock swing value. CIC increases linearly with the number of transfers as seen from comparing CIC on two CCDs of different sizes (3200 vs. 450 transfers). Right: simulated and measured CIC for the AstroSkipper. The number of transfers (3200 per amplifier), the horizontal clock width, and the filter (RC filter with $\tau = 5.1 \mu\text{s}$) are fixed. The model assumes Poisson statistics. We only consider variation in the horizontal clock swing which causes the highest electron rate generation compared to vertical and transfer gate clocks. We measure better than $\sim 10\%$ agreement between model and data for $\Delta H > 7.5 \text{ V}$.

full-well capacity suitable for the expected signal levels from SIFS ($\lesssim 1000 e^-$ for science images and $> 40,000 e^-$ for calibration products). Figure 13 shows the full-well capacity for increasing ΔH (top), which approaches levels comparable to other thick, fully depleted CCDs (Flaugher et al. 2015), and the CIC levels expected for each full-well (bottom). We measure an upper limit on the CIC using the low-voltage configuration from SENSEI (red arrow in Figure 13, bottom panel); however, the full-well capacity at these voltages ($\sim 900 e^-$) is inadequate for the SIFS application. In our optimization tests, we find that a CIC rate of $\sim 1 e^- \text{ pixel}^{-1} \text{ frame}^{-1}$ is possible with a corresponding full-well of $\sim 10,000 e^-$, which is adequate for the expected signal levels in science data products. However, we expect signals of $\sim 40,000\text{--}50,000 e^-$ in calibration data products. Configuring voltages for these signal level results in a CIC rate of $\sim 3 e^- \text{ pixel}^{-1} \text{ frame}^{-1}$. The achieved CIC rate for the high-voltage configuration is an unacceptable source of noise if the expected signals are in the order of a few electrons. We note that it might be possible to maintain a large full-well capacity while retaining low CIC to levels ($\lesssim 10^{-3} e^- \text{ pixel}^{-1} \text{ frame}^{-1}$) by employing waveform shaping (e.g., Barak et al. 2022). Shaping the clock pulse rise time and sharpness, which play a critical role in CIC generation, has been shown to reduce CIC in EMCCDs (Wilkins et al. 2014; Kyne et al. 2016).

This is the first time that full-well capacities of $\sim 40,000\text{--}50,000 e^-$ have been demonstrated with a Skipper CCD. This was achieved in a configuration with a horizontal clock swing, $\Delta H = 9.5 \text{ V}$, a vertical clock voltage swing, $\Delta V = 5 \text{ V}$, and a transfer gate clock voltage swing, $\Delta T = 5 \text{ V}$. We discovered that the floating sense node reference voltage can be a limitation in increasing the dynamic range. Furthermore, it is important to optimize this reference voltage for both full-well and “skipping” functionality. In the Skipper CCD output stage, the charge packet is passed to the small capacitance, floating sense node where the charge packet is read out once. Then the summing well voltage is set to the low state, i.e., lower than the sense node fixed reference voltage, for the charge packet to move back to the summing well, repeating this “skipping” process N_{samp} times. We optimized the sense node reference voltage to achieve the targeted full-well while maintaining the ability for photon-counting.

7. Conventional Characterization Tests

The implementation of conventional CCD characterization tests is important to evaluate the performance of the AstroSkipper CCDs. These tests not only allow us to assess the performance of individual AstroSkipper detectors in order to select the best detectors for SIFS, but also serve the broader purpose of comparing the AstroSkipper to other thick, fully

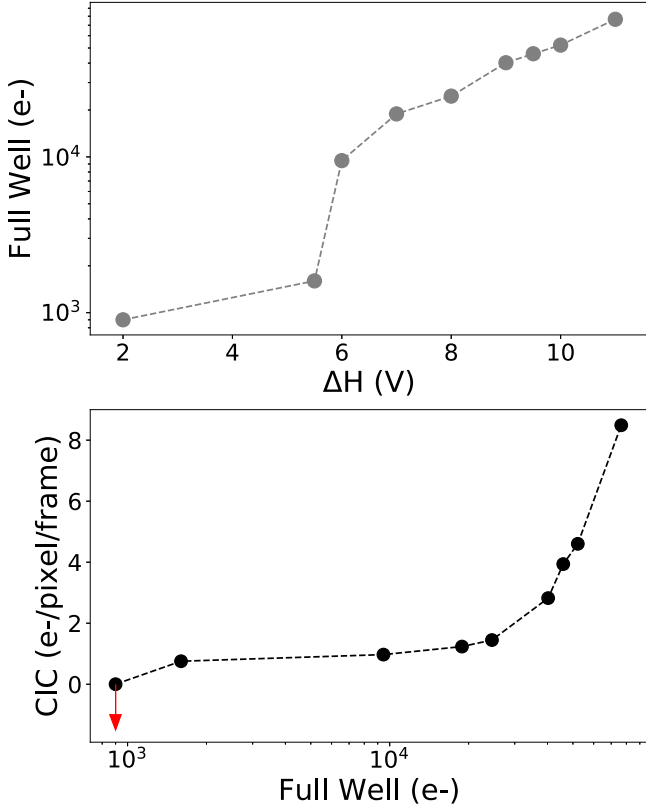


Figure 13. Top: full-well capacity as a function of the horizontal clock voltage swing (ΔH). Bottom: CIC event rate vs. full-well capacity. We measure an upper limit on the CIC (red arrow) with the SENSEI voltage configuration ($1.45 \times 10^{-3} \text{ e}^- \text{ pixel}^{-1} \text{ frame}^{-1}$), resulting in a full-well $\sim 900 \text{ e}^-$. Increasing the horizontal clock swing to $\Delta H = 6 \text{ V}$ increases full-well capacity to $\sim 10,000 \text{ e}^-$ at a CIC rate of $\sim 1 \text{ e}^- \text{ pixel}^{-1} \text{ frame}^{-1}$ and for $\Delta H = 9.5 \text{ V}$ we obtain a CIC rate of $\sim 3 \text{ e}^- \text{ pixel}^{-1} \text{ frame}^{-1}$ and a full-well capacity $> 40,000 \text{ e}^-$.

depleted CCD devices used in astronomical applications. For example, we demonstrate comparable metrics for CTI, DC, BFE, detector cosmetics, charge diffusion and QE between the AstroSkipper and well-characterized detectors used for DECam and DESI.

7.1. Charge Transfer Inefficiency

To characterize CTI, we implement the extended pixel edge response method (EPER). EPER consists of measuring the amount of deferred charge found in the extended pixel region or overscan of a flat-field at a specific signal level. CTI is calculated from the EPER as

$$\text{CTI} = \frac{S_D}{S_{LC} N_P}, \quad (7)$$

where S_D is the total deferred charge measured in the overscan in electrons, S_{LC} is the signal level (e^-) of the last column in the detector's activated area and N_P is the number of pixel

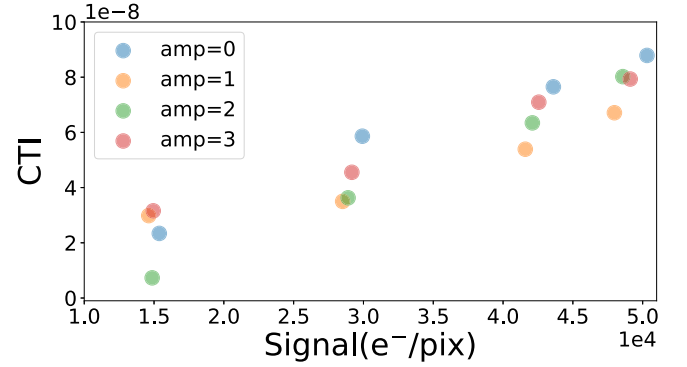


Figure 14. Average CTI vs. signal for four amplifiers in one of the selected AstroSkippers. The average CTI for all 24 amplifiers is 3.44×10^{-7} .

transfers in the serial register (Janesick 2001). For our CTI measurement, we take a number of flat-fields at increasing illumination levels ($\sim 10,000 \text{ e}^-$ to $\sim 50,000 \text{ e}^-$); Figure 14 shows the average CTI for all of the amplifiers in one of the AstroSkippers versus signal level. We calculate an average CTI value of 3.44×10^{-7} from the 24 amplifiers on the six astronomy-grade AstroSkipper CCDs, which is about an order of magnitude lower compared to the one we reported previously in Drlica-Wagner et al. (2020). Studies of deferred charge at low signal levels in Skipper CCDs are ongoing and are left to future work.

7.2. Dark Current

We use DC to refer to the electron events generated in the CCD during exposure and readout phases of data collection. These electron events are unrelated to the transfer of the charge between pixels (CIC). We note that the DC value reported for the AstroSkipper is an upper bound as it includes contributions from light leaks and other environmental sources.

The measurements of DC consist of acquiring 10 single-sample dark exposures with 400 s of exposure time. A combined dark, consisting of the median from 10 images, is calculated to remove cosmic rays and any transient effect; the combined dark is overscan subtracted and the signal mean is calculated over the activated area, divided by the exposure time, and normalized by the detector's gain. We measure DC values of $\sim 2 \times 10^{-4} \text{ e}^- \text{ pixel}^{-1} \text{ s}^{-1}$ for the six astronomy-grade AstroSkippers. Despite the fact that we tested the AstroSkippers in a dark room, light leaks dominate the electron event rates in our DC measurements and increase linearly with exposure and readout time. Previous DC measurements for astronomy performed with a similar setup in ambient lighting yielded DC values an order of magnitude higher ($\sim 10^{-3} \text{ e}^- \text{ pixel}^{-1} \text{ s}^{-1}$; Villalpando et al. 2022).

Barak et al. (2020) reports a significantly lower DC value of $6.82 \times 10^{-9} \text{ e}^- \text{ pixel}^{-1} \text{ s}^{-1}$ for a Skipper CCD operating underground (the lowest DC value measured for a CCD to date). In contrast to our measurements, the DC measurements reported in Barak et al. (2020) are performed underground with a Skipper CCD that is shielded from environmental radiation. For detectors with single-photon capabilities, external effects that increase the dark rate even by a small amount can be a problematic source of noise in the low-signal regime.

7.3. Photon Transfer Curve and Brighter-fatter Effect

The PTC characterizes the response of a CCD to illumination and can be used to measure the detector's gain and dynamic range. A PTC is constructed by taking several flat-fields at increasing illumination levels, which can then be used to show how the variance in the signal changes with the mean flux level of uniformly illuminated images. To eliminate non-uniformities, e.g., variations in the illumination and CCD cosmetic defects, the PTC is calculated with the difference between pairs of flat-fields.

It is assumed that charge collection in pixels exactly follows Poisson statistics, and therefore, pixels are independent light collectors. In this idealized case, the variance versus the signal mean should be linear, once the readout noise is negligible, with a $1/\text{gain}$ slope until pixel saturation. However, at high signal levels this assumption breaks, causing a loss in variance as the PTC linear behavior flattens out. Furthermore, binning neighboring pixels improves the linearity of the PTC (Downing et al. 2006; Astier et al. 2019). This indicates that correlation arises between neighboring pixels as charges migrate from one pixel to another, producing transverse electric fields on incoming photocharges (Holland et al. 2014). The repulsion effect between photocharges in a pixel's potential well causes quasistatic changes in the effective pixel area, for astronomical observations, biasing the light profile from a bright source. This effect is known as the BFE, which can bias the point-spread function (PSF) from a source by $\sim 1\%$ and the shear of faint galaxies, posing an unacceptable systematic for large imaging surveys if not corrected (Gruen et al. 2015; Lage et al. 2017; Coulton et al. 2018; Astier et al. 2019; Astier & Regnault 2023). At the detector level the BFE has been observed on DECam, Hyper Suprime-Cam, and LSSTCam fully depleted CCDs (Gruen et al. 2015; Astier et al. 2019; Astier & Regnault 2023). Astier et al. (2019) proposes an electrostatic model to characterize the time-dependent build-up of correlations in flat-fields. The model describes the resulting correlation between pixels that grow with increasing flux and decay rapidly as photocharges migrate to neighboring pixels, resulting in a loss of covariance. The covariance function, that describes the change in the effective area as a result of BFE, for

a given signal level (μ), is given by

$$C_{ij}(\mu) = \frac{\mu}{g} \left[\delta_{i0} \delta_{j0} + a_{ij} \mu g + \frac{2}{3} (\mathbf{a} \otimes \mathbf{a} + \mathbf{ab})_{ij} (\mu g)^2 + \frac{1}{6} (2\mathbf{a} \otimes \mathbf{a} \otimes \mathbf{a} + 5\mathbf{a} \otimes \mathbf{ab})_{ij} (\mu g)^3 + \dots \right] + \frac{n_{ij}}{g} \quad (8)$$

where a_{ij} describes the strength of the changes in the pixel area due to the accumulated charge and has units of $1/\text{e}^-$, b_{ij} describes other contributions to the pixel area change, e.g., shortened drift time and asymmetries in how charges are stored in pixels, g is the detector's gain, n_{ij} is a matrix that contains noise components with n_{00} being the traditional readout noise, and \otimes refers to the discrete convolution. We follow the method in Astier et al. (2019) and perform the fit for our covariance function up to signal values close to saturation ($\sim 8 \times 10^6$ ADUs) up to $O(a^{10})$ terms, resulting in a 11×11 covariance matrix as a function of mean signal from the difference of flat-field pairs, taken at an increasing illumination level. Figure 15 shows the recovered 11×11 a_{ij} and b_{ij} pixel matrices. We note that $|a_{00}| > a_{ij}$, therefore a_{00} is the biggest contributor to pixel change, i.e., the quantity that describes the strength of the BFE (Astier et al. 2019; Astier & Regnault 2023). In Figure 16, we show the a and b matrices best-fit values averaged over all amplifiers from an AstroSkipper detector as a function of distance with error bars representing the uncertainty from all the averages. We see that a decays rapidly and becomes isotropic; similarly to Astier et al. (2019), we see that b is negative except for b_{01} , which might indicate a parallel distance increase in the charge cloud as charge accumulates.

Astier et al. (2019) fit the electrostatic model (Equation (8)) for a LSST Teledyne e2V 250 device with a thickness of $100 \mu\text{m}$, operated at a substrate voltage of 70 V. They find $|a_{00}| = 2.377 \times 10^{-6}$. Astier & Regnault (2023) perform a BFE analysis for the CCDs in the Hyper Supreme-Cam, which uses deep-depleted, $200 \mu\text{m}$ thick Hamamatsu CCDs, operated with a substrate voltage of < 50 V (Miyazaki et al. 2017); they measure $|a_{00}| = 1.24 \times 10^{-6}$. We measure an average value of $|a_{00}| = 6.153 \times 10^{-6}$. We note that the AstroSkipper a_{00} higher value might be due to the thickness ($250 \mu\text{m}$) and the operating substrate voltage (40 V) as explained by a physics-based model from Holland et al. (2014), which shows that the PSF size depends on detector thickness and substrate voltage.

For spectroscopy, especially applications where the line's structure profile is important, i.e., the radial velocity structure of radiative transfer effects in an object (Schmid 2012), the BFE can be an important systematic. Furthermore, as part of spectroscopic data reduction, sky subtraction and wavelength calibration depend on sky lines and calibration lamp data, which often have a signal level that is significantly higher than the science data, sometimes approaching the detector's full-well capacity. This situation could potentially bias science

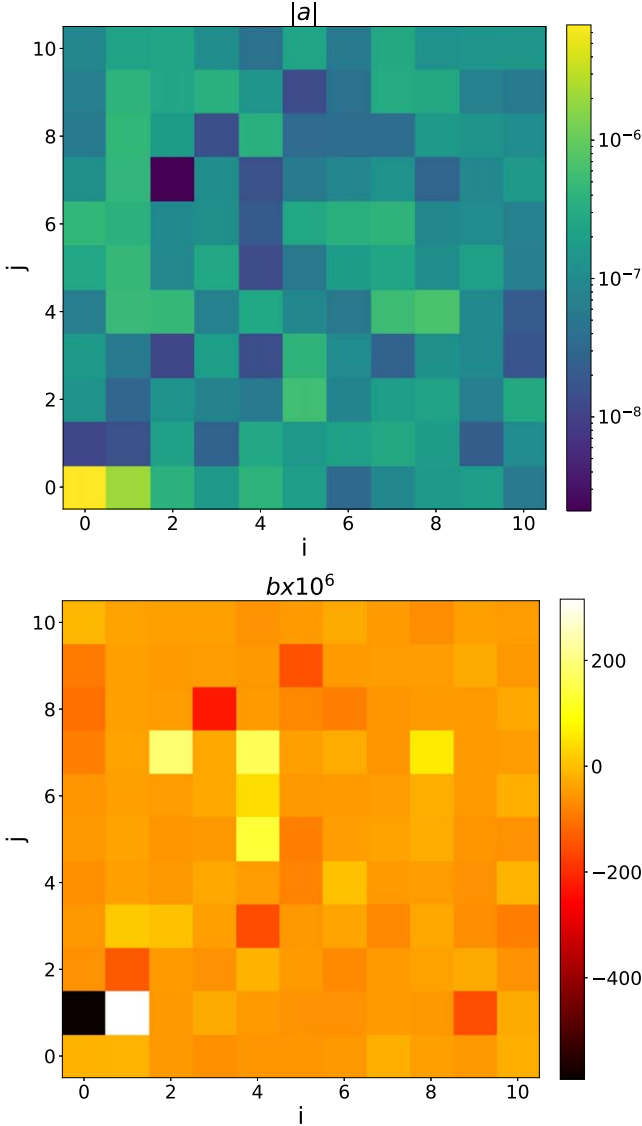


Figure 15. Top: measured a_{ij} from the electrostatic model (Equation (8)). Bottom: measured b_{ij} from Equation (8). Both matrices come from the fit to the electrostatic model using the method described in Astier et al. (2019). We measure an average value for a_{00} of $a_{00} = -6.153 \times 10^{-6} 1/e^-$. This factor dominates the pixel area change as charge accumulates (biggest contribution to the BFE). We note the asymmetric correlation between neighboring pixels ($a_{10}/a_{01} \sim 2.51$) due to the difference in pixel boundaries between the row and column directions (Coulton et al. 2018).

measurements due to the BFE. We note that further studies of the BFE in the context of spectroscopy are needed to fully determine how the BFE may bias various spectroscopic measurements, e.g., redshift recovery, equivalent widths, velocity dispersion, etc. For instance, assuming that DESI detectors will have similar BFE characteristics to those measured in the AstroSkipper, it would be possible to use DESI data to measure the impact of the BFE on DESI science

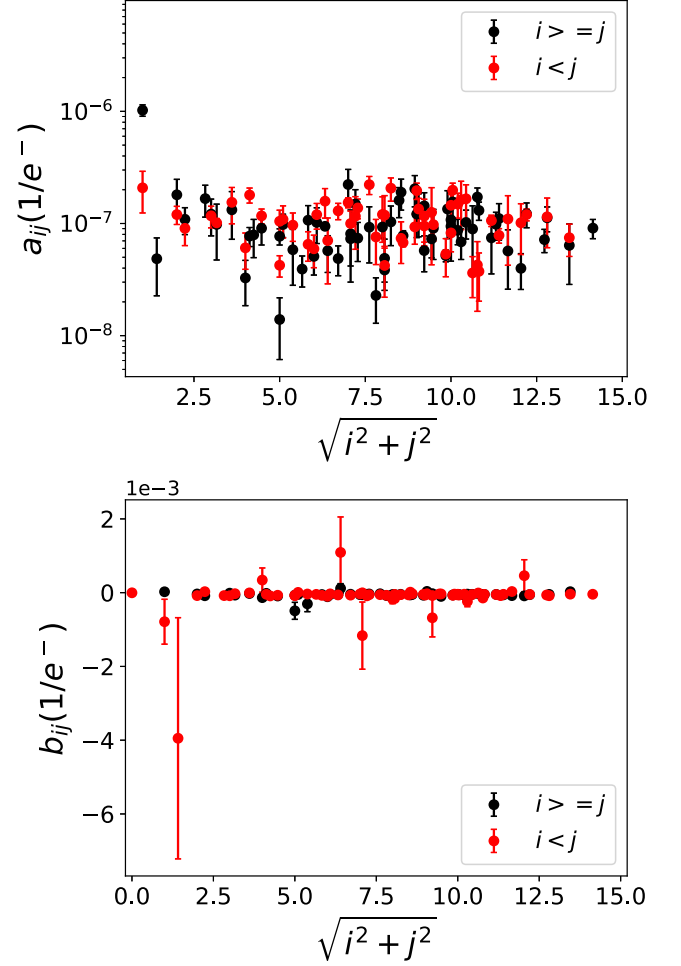


Figure 16. Best fit values from the a and b matrices, averaged over all amplifiers, as a function of distance. a decreases sharply and behaves isotropically for >3 pixels. Similarly to Astier et al. (2019), we see that values for b are negative except for b_{01} .

and predict the potential impact of the BFE on future spectroscopic cosmology surveys (e.g., a Stage-V spectroscopic survey; Schlegel et al. 2022).

The shape of the PTC curve (variance versus signal mean) can be approximated by considering the first element (the variance) in the covariance matrix, i.e., C_{00} and a_{00} in the Taylor expansion of Equation (8). The PTC curve as a function of μ with g , n_{00} , and a_{00} as fit parameters is given by

$$C_{00}(\mu) = \frac{1}{2g^2 a_{00}} [\exp(2a_{00}\mu g) - 1] + \frac{n_{00}}{g^2}. \quad (9)$$

Figure 17 shows a PTC curve for one of the AstroSkippers calculated with Equation (9). We implement public code from the LSST Science Pipelines for calculating and fitting the PTC (Bosch et al. 2018). We use 135 pairs of flat-fields, to compute the difference between them, taken at increasing signal rates

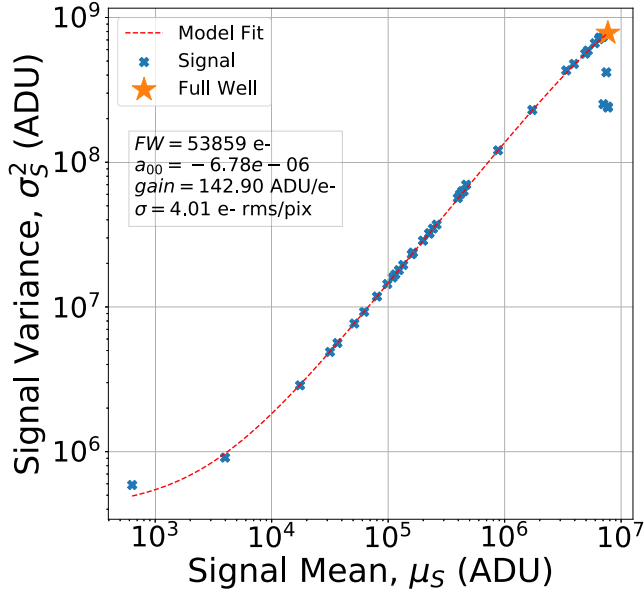


Figure 17. Photon Transfer Curve for one AstroSkipper amplifier. The PTC follows the model described by Equation (9) (Astier et al. 2019) and gives the BFE strength factor, a_{00} , from the covariance matrix. One can also calculate the detector’s gain from the model fit, which is given by the slope of the curve. The full-well capacity (orange star), is defined as the last “surviving” data point after applying an outlier rejection algorithm.

from a few electrons to saturation ($\sim 50,000 e^-$ for the AstroSkipper PTC shown in Figure 17). PTCs are constructed using $\Delta H = 9.5 \text{ V}$ and the full-well capacity is determined by the last data point that is not cut by the outlier rejection algorithm; the algorithm assigns weights to data points based on residuals from deviations to the model. Figure 18 shows the full-well capacity averaged across amplifiers for the six astronomy-grade AstroSkipper detectors; we measure full-well values ranging from $\sim 40,000 e^-$ to $65,000 e^-$ which are suitable for the SIFS application.

7.4. Cosmetic Defects

Cosmetic defect tests consist of characterizing pixels that are “hot” in dark exposure frames and “cold” in flat-fields at different illumination levels. We take 10 dark exposure frames with 400 s of exposure in the dark to measure bright pixels. Images are overscan-subtracted and sigma clipped to eliminate cosmic rays. We flagged bad pixels as those with mean values $\mu \pm 3.5\sigma$. The same statistical discrimination is applied for “cold” pixels in flat-fields, which also eliminates “hot” pixels that might be present ($\mu + 3.5\sigma$). We use different illumination levels up to $\mu \sim 30,000 e^- \text{ pixel}^{-1}$. We create a mask to include these pixels (“cold” and “hot”) and apply it to the images for subsequent tests. Figure 19 shows cosmetic values (the fraction of “cold” and “hot” pixels with respect to the total number of pixels in the detector) for all amplifiers in the six

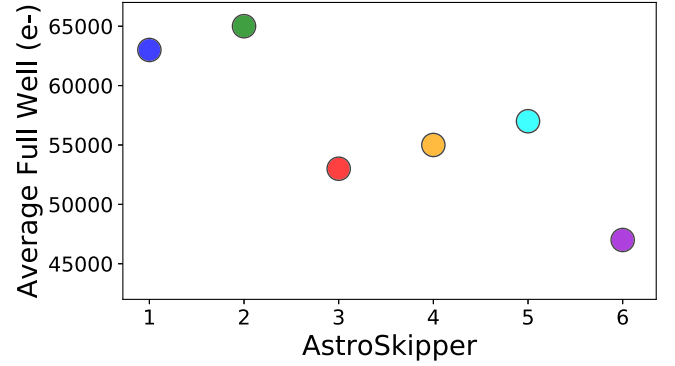


Figure 18. Average full-well capacity for the six detectors. Full-well measurements are calculated by the amplifier through the PTC; we average these full-well values from all amplifiers in a detector.

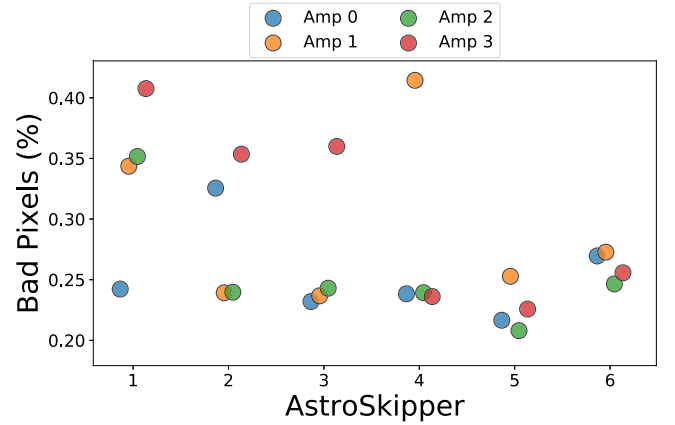


Figure 19. Percentage of “bad” pixels (“hot” and “cold” pixels) with respect to 1.92×10^6 pixels per amplifier. We find $<0.45\%$ bad pixels for all amplifiers; these pixels are removed in characterization tests.

AstroSkipper CCDs. We find cosmetic defects affect $<0.45\%$ of the pixels for all amplifiers.

7.5. Charge Diffusion

To characterize charge diffusion, we implement the method described in Lawrence et al. (2011) which is suitable for thick, backside illuminated, fully depleted CCDs. The method consists of exposing the CCD to low-energy X-rays from a ^{55}Fe source and statistically characterizing the charge clouds that result from the X-ray photon generating charge carriers in tight clusters. The charge diffuses laterally, producing a cloud with a Gaussian profile. The method uses the profile of the two-dimensional, Gaussian PSF to measure diffusion from these charge clouds. The pixel selection algorithm reconstructs events and selects those originating from conversions of 5.988 keV Mn $K\alpha$ photons, producing 1590 electron–hole pairs. The algorithm (1) defines a “box” that is 2×2 pixels and

calculates the charge in that region, (2) calculates local maxima by rejecting the box with minimum charge between two intersecting regions, (3) histograms remaining boxes, and (4) centers the window on the Mn $K\alpha$ peak position with upper bound at the $K\alpha$ and $K\beta$ peaks. We take 10 images each with 5 minutes exposure to ^{55}Fe radiation, which are combined to measure the PSF of the charge clouds using the method described above. We test different bias substrate voltages ranging from 30 to 70 V and compute the PSF as a function of the substrate voltage. We decide to operate the AstroSkipper CCD at 40 V (similar to DECam; Diehl et al. 2008), since we find that cosmetic defects, e.g., hot columns, grow with increasing substrate voltage (>40 V). We measure PSF values for all amplifiers $<6.75\ \mu\text{m}$ for the six AstroSkippers, operating with a substrate voltage of 40 V. This is comparable to DECam charge diffusion requirements: PSF $<7.5\ \mu\text{m}$ with a substrate voltage of 40 V (Diehl et al. 2008).

7.6. Absolute Quantum Efficiency

The LBNL Microsystems Laboratory CCD backside treatment and AR coating provides excellent ($\text{QE} > 80\%$) long wavelength (NIR) and acceptable ($\text{QE} > 60\%$) g-band response for $250\ \mu\text{m}$ thick detectors (e.g., Diehl et al. 2008; Bebek et al. 2017). In Drlica-Wagner et al. (2020), we demonstrated that a $250\ \mu\text{m}$ thick, backside illuminated Skipper CCD can achieve relative $\text{QE} > 75\%$ for wavelengths 450–900 nm. Here we report the first absolute QE measurements for astronomy-grade Skipper CCDs and demonstrate better QE than previous measurements.

We define the absolute QE as the ratio of the number of electrons generated and captured per incident photon at a given wavelength for a given unit area,

$$\text{QE}(\lambda) = (N_{\text{ADU}}K) \frac{hc}{P t_{\text{exp}} \lambda}, \quad (10)$$

where N_{ADU} is the signal from the detector in ADU, g is the detector's gain in ADU/e^- , h is the Planck constant, c is the speed of light, P is the incident optical power at the CCD surface, t_{exp} is the exposure time used to take the flat-fields, and λ is the incident light wavelength. An accurate measurement of the absolute QE depends on an accurate determination of the incident optical power at the AstroSkipper, housed in the vacuum dewar (Figure 3). To measure the absolute incident power at the detector, we mount a Thorlabs NIST traceable calibrated Si photodiode, with a $10\ \text{mm} \times 10\ \text{mm}$ activated area, on an AstroSkipper package (Figure 2). The photodiode plus AstroSkipper package is mounted inside the vacuum dewar at the same location that the AstroSkipper CCDs are mounted when testing.

Figure 20 shows the absolute QE for one quadrant of an AstroSkipper and the comparison with DECam and DESI detectors. We see good agreement with the QE of the DESI

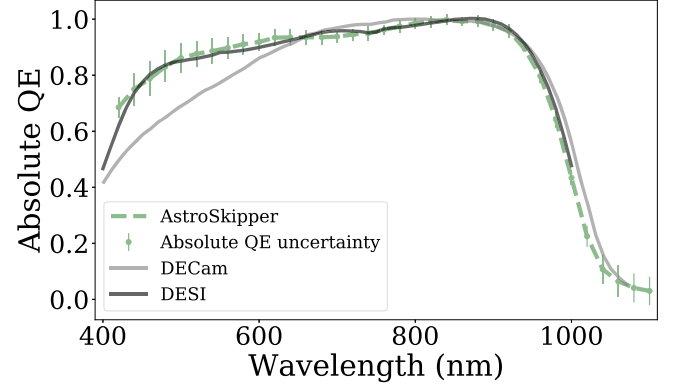


Figure 20. Absolute quantum efficiency for one AstroSkipper's amplifier compared to absolute QE from DECam detectors (dark gray line) (Diehl et al. 2008) and relative QE from DESI detectors (gray line). Error bars in the AstroSkipper absolute QE represent the uncertainty in the absolute calibration at each wavelength. We see excellent agreement with DESI detector's QE (the AstroSkipper and DESI NIR detectors are $\sim 250\ \mu\text{m}$ thick and have similar AR coating from LBNL Microsystems Laboratory). We measure $\text{QE} \gtrsim 80\%$ for 450 nm and 980 nm and $\text{QE} > 90\%$ for wavelengths from 600 to 900 nm for all AstroSkippers; this is an improvement from the first Skipper CCD relative QE measurements ($\text{QE} > 75\%$ between 450 and 900 nm) we reported in Drlica-Wagner et al. (2020).

detectors, which is expected given that the AstroSkipper has a similar AR coating (Bebek et al. 2017). For all amplifiers in the six AstroSkippers, we see $\text{QE} \gtrsim 80\%$ between 450 and 980 nm, and $\text{QE} > 90\%$ for wavelengths from 600 to 900 nm.

We note that the absolute calibration, i.e., the ratio of the incident optical power in the Thorlabs photodiode relative to the Oriel NIST traceable photodiode on the integrating sphere (Figure 3) is the greatest source of uncertainty; therefore, we take multiple absolute calibration measurements. We derive an uncertainty in the absolute QE at each wavelength; we find uncertainties $<6\%$ in the absolute QE values for all wavelengths. Error bars in Figure 20 represent the uncertainty at each wavelength calculated from the absolute calibration measurements.

8. Summary and Discussion

We have presented the results from characterizing and optimizing eight AstroSkipper CCDs developed for a prototype Skipper CCD focal plane for SIFS. We identified six astronomy-grade detectors that pass requirements to be used in the SIFS AstroSkipper CCD focal plane; Table 1 summarizes characterization measurements derived from all amplifiers on these six detectors. Measurements satisfied targeted goals, which were set by previous characterization of DESI detectors (Bonati et al. 2020).

An important conclusion from the characterization and optimization of the AstroSkipper is that CIC is a critical issue if large full-well capacities are required. While we achieve a low

Table 1
Summary of the AstroSkipper Characterization Results for the Six Out of Eight Devices with Best Performance

Parameter	Goal	Measured	Units
Single-sample Readout Noise ($N_{\text{samp}} = 1$)	3.5	<4.3	e^- rms pixel $^{-1}$
Multi-sample Readout Noise ($N_{\text{samp}} = 400$)	0.18	0.18	e^- rms pixel $^{-1}$
Cosmetic Defects	10%	<0.45%	...
Dark Current	$<8 \times 10^{-3}$	2×10^{-4}	e^- pixel $^{-1}$ s $^{-1}$
Clock-induced Charge	1.52×10^{-4}	3	e^- pixel $^{-1}$ frame $^{-1}$
Full-well Capacity	>40,000	$\sim 40,000$ –60,000	e^-
Nonlinearity	<1.5%	<0.05% and <1.5% (low signals)	...
Charge Transfer Inefficiency	$<1 \times 10^{-5}$	3.44×10^{-7}	...
Charge Diffusion (PSF)	<15	<7.5	μm
Absolute Quantum Efficiency	>80%	$\gtrsim 80\%$ (450–980 nm); $\gtrsim 90\%$ (600–900 nm)	...

CIC of $<1.45 \times 10^{-3} e^- \text{ pixel}^{-1} \text{ frame}^{-1}$ at a full-well capacity of $\sim 900 e^-$, this rises to $\sim 1 e^- \text{ pixel}^{-1} \text{ frame}^{-1}$ at a full-well capacity of $\sim 10,000 e^-$ and $\sim 3 e^- \text{ pixel}^{-1} \text{ frame}^{-1}$ at a full-well capacity of $>40,000 e^-$. This prompts a nuanced consideration of the trade-off between full-well capacity and CIC, especially when optimizing the system for the expected signal level in the SIFS application. For example, one can think of configuring the system with high-voltage swings for calibration data products where signal levels are expected to be $>40,000 e^-$, and subsequently transitioning to a lower voltage swing configuration for science data products, where signals are $\lesssim 1000 e^-$. Future approaches to reducing CIC in Skipper CCDs will explore waveform shaping solutions, which have been shown to reduce CIC in EMCCDs (e.g., Wilkins et al. 2014; Kyne et al. 2016). In addition, we find that because CIC is generated primarily in the serial register, the length of the serial registers should be considered carefully when designing Skipper CCDs.

The voltage optimization of the AstroSkipper is especially significant in attaining an appropriate full-well capacity for the intended application; we demonstrated that Skipper CCDs can achieve full-well capacities $>40,000 e^-$ while maintaining the ability to count photons as demonstrated by the achieved sub-electron readout noise of $\sigma_{400} = 0.18 e^- \text{ rms pixel}^{-1}$ with 400 non-destructive measurements of the charge in each pixel. Furthermore, we highlight the absolute QE measurements (QE $\gtrsim 80\%$ between 450 and 980 nm, and QE $> 90\%$ for wavelengths from 600 to 900 nm). This is an improvement relative to previous Skipper CCD QE measurements and is comparable to the QE of the DESI red-channel detectors (Bebek et al. 2017).

We demonstrated that the AstroSkippers have a CTI of $\sim 10^{-7}$ at high signal levels ($\geq 10,000 e^-$) using the EPER method (Section 7.1). However, it has been recognized that the fractional deferred charge can be higher at low signal levels due to charge trapping (e.g., Snyder & Roodman 2019). Ongoing studies in the context of DM experiments are leveraging the single-electron counting capabilities of Skipper CCDs to study how charge traps induced by lattice defects might be

responsible for deferred charge seen at low signal levels. These studies use the pocket pumping technique (Janesick 2001; Mostek et al. 2010; Cervantes-Vergara et al. 2023) to estimate the density, intensity, and emission time constants of charge traps. One of the primary goals of the charge trap characterization is to identify (and mitigate) chemical impurities and lattice defects from different fabrication processes that could be causing these traps. The results of these studies and the impact of charge traps on deferred charge at low signal levels will be presented in future work.

We achieved a factor of five reduction in the readout time (from $200 \mu\text{s pixel}^{-1}$ to $40 \mu\text{s pixel}^{-1}$ for the entire pixel sequence). We emphasize that readout time reduction is critical in Skipper CCD astronomy applications. Current efforts to achieve low Skipper CCD readout times are ongoing at Fermilab and LBNL. Firmware modifications to the LTA have demonstrated improved readout times ($\sim 5.1 \mu\text{s pixel}^{-1} \text{ sample}^{-1}$) for a Skipper CCD with a single-sample readout noise of $\sim 10 e^- \text{ rms pixel}^{-1}$ (Lapi et al. 2022). Current work is ongoing to optimize readout noise at low readout times. Novel multi-amplifier sensing (MAS) Skipper CCD designs represent an attractive solution to reducing readout times (Botti et al. 2023; Holland 2023). MAS devices are loosely based on the distributed gate amplifier concept (Wen et al. 1975) and consists of a serial register with M floating-gate amplifiers in series. Importantly, the readout time improvement from a MAS device goes as $\sim 1/M$ when compared to a single floating-gate amplifier from a conventional Skipper CCD. Furthermore, the ability to reduce the single-sample readout noise would reduce the number of samples needed to achieve photon-counting, lowering readout times. Because the noise reduction in MAS devices scales as $1/\sqrt{M}$ for a single-sample readout by each amplifier, one can increase the number of on-chip Skipper amplifiers to achieve better single-sample noise. Current work at Fermilab is ongoing to develop readout electronics that are scalable to thousands of channels (Chierchie et al. 2023), which would be suitable for a future MAS device. Efforts are underway to characterize 16-amplifier, backside treated, and AR coated MAS devices using procedures similar to those described here.

Acknowledgments

The fully depleted Skipper CCD was developed at Lawrence Berkeley National Laboratory, as were the designs described in this work. E.M.V. acknowledges support from the DOE Graduate Instrumentation Research Award and the DOE Office of Science Graduate Student Research Award. The work of A. A.P.M. was supported by the U.S. Department of Energy under contract No. DE-244 AC02-76SF00515. This work was partially supported by the Fermilab Laboratory Directed Research and Development program (L2019.011 and L2022.053). Support was also provided by NASA APRA award No. 80NSSC22K1411 and a grant from the Heising-Simons Foundation (No. 2023-4611). This manuscript has been authored by the Fermi Research Alliance, LLC, under contract No. DE-AC02-07CH11359 with the US Department of Energy, Office of Science, Office of High Energy Physics. The publisher, by accepting the article for publication, acknowledges that the United States Government retains a non-exclusive, paid-up, irrevocable, worldwide license to publish or reproduce the published form of this manuscript, or allow others to do so, for United States Government purposes.

ORCID iDs

Edgar Marrufo Villalpando  <https://orcid.org/0000-0002-8169-8855>

Alex Drlica-Wagner  <https://orcid.org/0000-0001-8251-933X>

Andrés A. Plazas Malagón  <https://orcid.org/0000-0002-2598-0514>

Marco Bonati  <https://orcid.org/0000-0001-5025-4963>

Luciano Fraga  <https://orcid.org/0000-0003-0680-1979>

References

- Aguilar-Arevalo, A., Bessia, F. A., Avalos, N., et al. 2022, arXiv:2202.10518
- Amelio, G. F., Tompsett, M. F., & Smith, G. E. 1970, *BSTJ*, 49, 593
- Arnquist, I., Avalos, N., Baxter, D., et al. 2023, *PhRvL*, 130, 171003
- Astier, P., Antilogus, P., Juramy, C., et al. 2019, *A&A*, 629, A36
- Astier, P., & Regnault, N. 2023, *A&A*, 670, A118
- Barak, L., Bloch, I. M., Botti, A., et al. 2022, *PhRvP*, 17, 014022
- Barak, L., Bloch, I. M., Cababie, M., et al. 2020, *PhRvL*, 125, 171802
- Bebek, C., Emes, J., Groom, D., et al. 2015, *JInst*, 10, C05026
- Bebek, C., Emes, J., Groom, D., et al. 2017, *JInst*, 12, C04018
- Bernstein, G. M., Abbott, T. M. C., Desai, S., et al. 2017, *PASP*, 129, 114502
- Bonati, M., Estrada, J., Castaneda, A., & Hernandez, P. 2020, *Proc. SPIE*, 11452, 114521L
- Bosch, J., AlSayyad, Y., Armstrong, R., et al. 2018, An Overview of the LSST Image Processing Pipelines in ASP Conf. Series. Astronomical Data Analysis Software and Systems XXVIII 523, ed. P. J. Teuben et al. (San Francisco: ASP), 521
- Botti, A. M., Cervantes-Vergara, B. A., Chavez, C. R., et al. 2023, arXiv:2308.09822
- Botti, A. M., Uemura, S., Moroni, G. F., et al. 2022, *PhRvD*, 106, 072005
- Boyle, W. S., & Smith, G. E. 1970, *BSTJ*, 49, 587
- Cancelo, G. I., Chavez, C., Chierchie, F., et al. 2021, *JATIS*, 7, 015001

- Cervantes-Vergara, B. A., Perez, S., Estrada, J., et al. 2023, *JInst*, 18, P08016
- Chandler, C. E., Bredthauer, R. A., Janesick, J. R., Westphal, J. A., & Gunn, J. E. 1990, *Proc. SPIE*, 1242, 238
- Chierchie, F., Chavez, C., Haro, M. S., et al. 2023, *JInst*, 18, P01040
- Chierchie, F., Moroni, G. F., Stefanazzi, L., et al. 2021, *PhRvL*, 127, 241101
- Coulton, W. R., Armstrong, R., Smith, K. M., Lupton, R. H., & Spergel, D. N. 2018, *AJ*, 155, 258
- Crisler, M., Essig, R., Estrada, J., et al. 2018, *PhRvL*, 121, 061803
- Daigle, O., Carignan, C., Gach, J.-L., et al. 2009, *PASP*, 121, 866
- Daigle, O., Quirion, P.-O., & Lessard, S. 2010, *Proc. SPIE*, 7742, 774203
- Damerell, C., Farley, F., Gillman, A., & Wickens, F. 1981, *NIMPR*, 185, 33
- de Oliveira, A. C., de Oliveira, L. S., Gneiding, C. D., et al. 2010, *Proc. SPIE*, 7739, 77394S
- Diehl, H. T., Angstadt, R., Campa, J., et al. 2008, *Proc. SPIE*, 7021, 702107
- Downing, M., Baade, D., Sinclair, P., Deiries, S., & Christen, F. 2006, *Proc. SPIE*, 6276, 627609
- Drlica-Wagner, A., Villalpando, E. M., O'Neil, J., et al. 2020, *Proc. SPIE*, 11454, 114541A
- Fernández Moroni, G., Estrada, J., Cancelo, G., et al. 2012, *ExA*, 34, 43
- Fernandez-Moroni, G., Harnik, R., Machado, P. A. N., et al. 2022, *JHEP*, 2022, 127
- Flaugher, B., Diehl, H. T., Honscheid, K., et al. 2015, *AJ*, 150, 150
- Gow, J. P. D., Murray, N. J., Holland, A. D., & Burt, D. 2014, *ITNS*, 61, 1843
- Gow, J. P. D., Wood, D., Murray, N. J., et al. 2016, *JATIS*, 2, 026001
- Groom, D. E., Haque, S., Holland, S. E., & Kolbe, W. F. 2017, *JAP*, 122, 055301
- Gruen, D., Bernstein, G. M., Jarvis, M., et al. 2015, *JInst*, 10, C05032
- Holland, S. 2023, *AN*, 344, e20230072
- Holland, S., Dawson, K., Palaio, N., et al. 2007, *NIMPA*, 579, 653
- Holland, S., Groom, D., Palaio, N., Stover, R., & Wei, M. 2003, *ITED*, 50, 225
- Holland, S. E., Bebek, C. J., Kolbe, W. F., & Lee, J. S. 2014, *JInst*, 9, C03057
- Janesick, J. R. 2001, Scientific Charge Coupled Devices, PM83 (Bellingham, WA: SPIE)
- Janesick, J. R., Elliott, T., Dingizian, A., Bredthauer, R. A., & Chandler, C. E. 1990, *Proc. SPIE*, 1242, 223
- Kyne, G., Hamden, E. T., Lingner, N., et al. 2016, *Proc. SPIE*, 9915, 991507
- Lage, C., Bradshaw, A., & Tyson, J. A. 2017, *JInst*, 12, C03091
- Lapi, A. J., Chierchie, F., Moroni, G. F., et al. 2016, *Proc. SPIE*, 12191, 121910V
- Lawrence, D., O'Connor, P., Frank, J., & Takacs, P. 2011, *PASP*, 123, 1100
- Lepine, J. R. D., de Oliveira, A. C., Figueredo, M. V., et al. 2003, *Proc. SPIE*, 4841, 1086
- Macanhan, V. B. P., Santoro, F. G., Gneiding, C. D., et al. 2010, *Proc. SPIE*, 7735, 77356R
- Miyazaki, S., Komiyama, Y., Kawanomoto, S., et al. 2017, *PASJ*, 70, S1
- Mostek, N. J., Bebek, C. J., Karcher, A., et al. 2010, *Proc. SPIE*, 7742, 774216
- Rauscher, B. J., Holland, S. E., Kan, E., et al. 2022, *Proc. SPIE*, 12180, 1218065
- Rodrigues, D., Andersson, K., Cababie, M., et al. 2021, *NIMPA*, 1010, 165511
- Schlegel, D. J., Ferraro, S., Aldering, G., et al. 2022, arXiv:2209.03585
- Schmid, H. 2012, Astronomical Imaging and Spectroscopy with CCD Detectors, ETH Zurich, Institute for Particle Physics and Astrophysics, <https://ethz.ch/content/dam/ethz/special-interest/phys/particle-physics/quanz-group-dam/documents-old-s-and-p/Courses/vp-asl-astro/CCDObservations.pdf>
- Snyder, A., & Roodman, A. 2019, *JATIS*, 5, 041509
- Tiffenberg, J., Sofó-Haro, M., Drlica-Wagner, A., et al. 2017, *PhRvL*, 119, 131802
- Tulloch, S. M., & Dhillon, V. S. 2011, *MNRAS*, 411, 211
- Villalpando, E. M., Drlica-Wagner, A., Bonati, M., et al. 2022, *Proc. SPIE*, 12191, 121910U
- Wen, D., Early, J., Kim, C., & Amelio, G. 1975, in 1975 IEEE Int. Solid-State Circuits Conf. Digest of Technical Papers, XVIII (Piscataway, NJ: IEEE), 24
- Wilkins, A. N., McElwain, M. W., Norton, T. J., et al. 2014, *Proc. SPIE*, 9154, 91540C
- Wood, D., Hall, D. J., Gow, J., et al. 2017, *ITNS*, 64, 2814